

## Article

# Influence of Metal Oxide Nanoparticles as Antimicrobial Additives Embedded in Waterborne Coating Binders Based on Self-Crosslinking Acrylic Latex

Denisa Steinerová <sup>1,\*</sup>, Andréa Kalendová <sup>1</sup>, Jana Machotová <sup>1</sup>, Petr Knotek <sup>2</sup>, Petr Humpolíček <sup>3</sup>, Jan Vajdák <sup>3</sup>, Stanislav Slang <sup>4</sup>, Anna Krejčová <sup>5</sup>, Ludvík Beneš <sup>6</sup> and Felipe Wolff-Fabris <sup>7</sup>

<sup>1</sup> Institute of Chemistry and Technology of Macromolecular Materials, Faculty of Chemical Technology, University of Pardubice, 532 10 Pardubice, Czech Republic

<sup>2</sup> Department of General and Inorganic Chemistry, Faculty of Chemical Technology, University of Pardubice, 532 10 Pardubice, Czech Republic

<sup>3</sup> Centre of Polymer Systems, Tomas Bata University in Zlín, 760 01 Zlín, Czech Republic

<sup>4</sup> Center of Materials and Nanotechnologies, Faculty of Chemical Technology, University of Pardubice, 532 10 Pardubice, Czech Republic

<sup>5</sup> Institute of Environmental and Chemical Engineering, Faculty of Chemical Technology, University of Pardubice, 532 10 Pardubice, Czech Republic

<sup>6</sup> Joint Laboratory of Solid State Chemistry, Faculty of Chemical Technology, University of Pardubice, 532 10 Pardubice, Czech Republic

<sup>7</sup> European Center for Dispersion Technologies, 95100 Selb, Germany

\* Correspondence: steinerovadenisa@gmail.com; Tel.: +420-727-843-211



**Citation:** Steinerová, D.; Kalendová, A.; Machotová, J.; Knotek, P.; Humpolíček, P.; Vajdák, J.; Slang, S.; Krejčová, A.; Beneš, L.; Wolff-Fabris, F. Influence of Metal Oxide Nanoparticles as Antimicrobial Additives Embedded in Waterborne Coating Binders Based on Self-Crosslinking Acrylic Latex. *Coatings* **2022**, *12*, 1445. <https://doi.org/10.3390/coatings12101445>

Academic Editor: Florina Branzoi

Received: 19 August 2022

Accepted: 26 September 2022

Published: 30 September 2022

**Publisher's Note:** MDPI stays neutral with regard to jurisdictional claims in published maps and institutional affiliations.



**Copyright:** © 2022 by the authors. Licensee MDPI, Basel, Switzerland. This article is an open access article distributed under the terms and conditions of the Creative Commons Attribution (CC BY) license (<https://creativecommons.org/licenses/by/4.0/>).

**Abstract:** This article deals with the simple preparation of environmentally friendly acrylic latex binders, which are functionalized with nanoparticles of metal oxides, namely MgO, ZnO, La<sub>2</sub>O<sub>3</sub> and combinations of MgO and ZnO, serving as functional components to achieve antimicrobial properties, but also to improve physical–mechanical properties and chemical resilience. The incorporation of uncoated powder nanoparticles was performed during the synthesis, using the two-stage semi-continuous emulsion radical polymerization technique, to obtain latexes containing 0.5%–1.3% nanoparticles relative to the polymer content. Changes in latex performance due to nanoparticles were compared from the point of view of the type and concentration of metal oxide nanoparticles in latex. The results of the tests showed that all types of nanoparticles showed very promising properties, while with increasing concentration of nanoparticles there was an improvement in properties. The nanoparticles in latex provided interfacially crosslinked transparent smooth coating films with high gloss and good physical–mechanical properties. Latexes containing the highest concentration of nanoparticles provided coatings with significant antimicrobial activity against all tested bacterial and fungal strains, but also in-can preservative stability of liquid latex. Furthermore, the coatings were resistant to solvents, and in addition, latexes with MgO nanoparticles showed a significant decrease in the minimum film-forming temperature, and latex with a concentration of about 1.3% MgO did not show any flash corrosion under the coating film cast on a steel substrate. The latexes containing MgO and La<sub>2</sub>O<sub>3</sub> nanoparticles provided coatings that were very resistant to water bleaching.

**Keywords:** keto-hydrazide crosslinking; ionic crosslinking; nanostructured magnesium oxide; zinc oxide and lanthanum oxide; antimicrobial activity

## 1. Introduction

Great efforts are currently being made to use environmentally friendly coatings [1–4], but at the same time, there is a growing demand for antimicrobial coatings worldwide [5–7], as evidenced by a large number of articles and patents [8–10]. Combining these two requirements is not an easy task, as one of the biggest trends in the market for green coatings is the introduction of low or zero volatile organic solvent (VOC) technologies, leading to the use

of waterborne or solvent-free coatings. Waterborne coatings are an excellent alternative to solvent-based coatings, as they are a universal, high-quality, and environmentally friendly choice that meets both European and US regulations that require VOCs to be below 350 g/L of water [11,12]. Acrylic latex paints are probably the most widely used commercially produced polymeric waterborne coatings [12,13], mainly due to their easy preparation and modification. In addition, they are characterized by low toxicity, high resistance to atmospheric conditions, fast drying at room temperature, and compatibility with a wide range of surfaces, such as metals, mineral substrates, or wood [14–16]. An equally important advantage is good usability for the target customer, thanks to easy washing with water (before curing) and low odor [17–19]. Due to these properties, they have become very popular despite their typical shortcomings, such as the formation of flash corrosion, and low resistance to high and low temperatures or solvents and water, which often limits their applicability [20–22].

One way to improve the durability of latex coatings is to crosslink polymer chains with covalent or ionic bonds [23,24]. Researchers have developed a number of crosslinking mechanisms for latex films [21,25,26], both two-pack and one-pack (self-crosslinking) compositions, with “two-pack in one pot” systems. The one-pack compositions are preferred, mainly for ease of use, as they do not require the addition of an external crosslinker, or the mixing of different latexes produced at different stages. In these systems, the crosslinking reaction is usually triggered either by a drastic decrease in pH or by evaporation of water during film drying [27,28]. A particularly effective crosslinking mechanism used in the “two-pack in one pot” latex compositions is based on a reaction between carbonyl groups in diacetone acrylamide repeat units (DAAM), which are part of the polymer chain, and hydrazide groups from adipic acid dihydrazide (ADH) dissolved in the aqueous phase (see Figure 1) [29–33]. The unique feature of this reaction is rapid curing at room temperature which further increases the barrier properties, mechanical properties, and water-repellent properties of coating films [31].

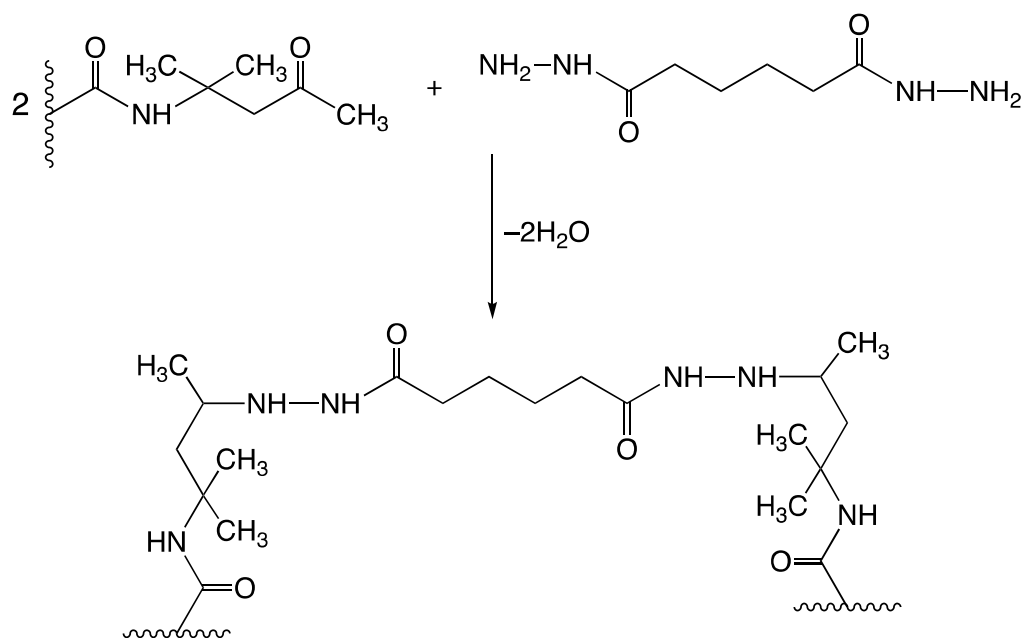


**Figure 1.** Crosslinking reaction between copolymerized diacetone acrylamide and adipic acid dihydrazide.

A serious drawback of waterborne coatings is that they are sensitive to biodegradation by bacteria and fungi while in the can, or later as an applied coating film [34,35]. Various inorganic and organic materials have been used for this purpose in the past, but many of them are now banned due to their harmfulness to human health or the environment [36–38] and thus non-compliance with relevant European legislation (the European Union specifically

adopted Directive 98/8/ES). Current findings stimulate further reductions in the number of substances with antimicrobial effects [35]. Therefore, new environmentally-friendly alternatives to antimicrobial protection should be sought [39,40], as microbial infectious diseases are a serious health and socio-economic problem which attracts the attention of the public around the world [41].

Nanoparticles provide a new approach to the development of antimicrobial materials [42,43]. In particular, metal oxide (MeO) nanoparticles have the potential to be effective against a wide range of microorganisms (MO), such as aerobic bacteria, anaerobic bacteria, viruses, yeasts, and fungi [5,44–47]. Metal cations are thought to destroy the enzymes of these MOs and are therefore unable to build up resistance [48–50]. An example of a promising MeO with an antimicrobial effect is nanostructured  $\text{La}_2\text{O}_3$  which has been found to inhibit the growth of bacteria, fungi, and yeast, and for this reason it was investigated in safety and biomedical applications [51]. Lanthanum is a rare-earth element possessing unique physical and chemical properties such as high density, high melting point, high thermal conductance, and conductivity, which provides the potential for enhancing the useful properties of the coating [52,53].

In addition to antimicrobial properties, MeO nanoparticles can also have a positive effect on the structural properties of the coating [54,55]. If limited soluble MeO nanoparticles are used, the properties of acrylic latex coatings can also be improved by ionic (physical) crosslinking with subsequent complex formation, which occurs in the interfacial zones between adjacent latex particles, through ionic dipolar interactions [24]. In the case of carboxy-functionalized latexes, ionic bonds are formed between carboxyl groups on the surface of latex particles in the presence of polyvalent metals or metal complexes [56–58]. ZnO (often reported in the relevant literature) appears to be a suitable crosslinker, as it is a sparingly soluble metal oxide that does not dramatically affect latex stability [59]. Ammonia, which is often used to ensure the stability of the latex system, reacts with zinc ions to form a zinc amine complex. Upon evaporation of ammonia and water in the film-forming process, zinc ions are released from the complex and react with the carboxyl groups on the surface of the latex particles at room temperature. The ionic crosslinking reaction is first formed between zinc ions and carboxyl groups and then transformed into a more thermodynamically stable coordinated complex (see Figure 2). This effect is attributed to rearrangement caused by kinetic factors, during a process in which latex particles collect to form a tighter arrangement [54]. Compared to conventional latexes, these compositions offer excellent thermal stability, hardness, resistance to water, weathering, etc. [60,61].

The problem of flash corrosion of latex coatings limits their use on metal substrates (especially steel), where the soluble iron salt is transferred to the coating film during drying [62]. In practice, this problem is solved using often toxic flash corrosion inhibitors, such as sodium benzoate or sodium nitrite [63,64]. The corrosion potential of the metal and the nature of corrosion are mainly dependent on the concentration of hydrogen ions in the aqueous medium (pH). Pourbaix diagrams can be used to predict the corrosion behavior of a metal substrate [65]. In the case of a steel substrate according to the Pourbaix diagram for iron, it can be expected that at a pH above 8.5 the steel passes into the passivity region and no iron oxidation occurs. Thus, the solution to this problem could be to alkalize the latex with an agent that will not leak during the drying process and will maintain a high pH (above 8.5) throughout the coating process. Nanostructured MgO appears to be a suitable candidate that dissociates into hydroxyl and magnesium ions in an aqueous medium, thus shifting the pH of the aqueous solution to the alkaline range [55,66,67].

Because of concern for human health and environmental protection, nanoparticles have begun to be investigated regarding their cytotoxicity. In general, the toxicity depends on nanoparticle size and concentration [68,69]. When comparing the cytotoxicity data available in the literature for nanostructured ZnO [70,71], MgO [72–74], and  $\text{La}_2\text{O}_3$  [75–77], ZnO, which has also been the most studied material, appears to be the most cytotoxic (with proven toxicity for aquatic organisms and human cells [78–85]), while MgO is considered the least harmful [73] with the possible use as an anti-cancer treatment agent [72].

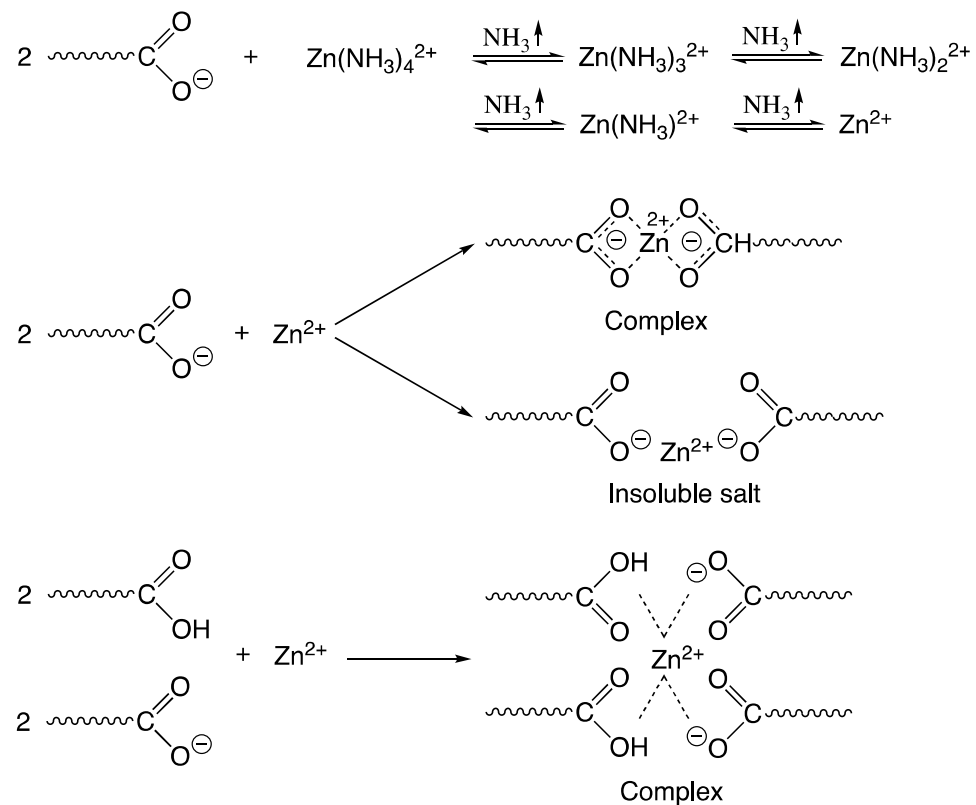


**Figure 2.** Crosslinking reaction between zinc ion and acidic functional monomer.

The aim of this paper is to present and compare surface untreated MeO nanoparticles (specifically MgO, ZnO, La<sub>2</sub>O<sub>3</sub>, and combinations of MgO and ZnO) in the role of multi-functional additives for hygienic acrylic latex coating binders. This study follows, complements, and extends our previous research [23,56,62,66]. To the best of our knowledge, the applications of La<sub>2</sub>O<sub>3</sub> nanoparticles, and combinations of nanostructured MgO and ZnO in latex coating compositions have not been presented so far. The effectiveness of the latexes was evaluated for biocidal effect with respect to the type of nanoparticles present and their concentration, both in the liquid binder (the in-can preservation stability) and their coating films. Several other benefits of using specific nanoparticles in the coating systems were highlighted.

## 2. Materials and Methods

### 2.1. Incoming Materials

The latexes were prepared from monomeric methyl methacrylate (MMA), n-butyl acrylate (BA), methacrylic acid (MAA) and diacetone acrylamide (DAAM) supplied by Sigma-Aldrich, Prague, Czech Republic. Adipic acid dihydrazide (ADH, active substance content > 98%; Sigma-Aldrich, Prague, Czech Republic) served as the crosslinking agent; Disponil FES 993 (anion-active surfactant based on sodium polyglycol ether sulfate; BASF, Prague, Czech Republic), as the emulsifier; ammonium persulfate (active substance content > 99.9%; Lach-Ner, Neratovice, Czech Republic), as the initiator; and nanostructured MeO with no surface treatment, as the antimicrobial and antifungal ingredient of the latex, namely (i) MgO nanoparticles with particle size < 200 nm (commercial name JR-NMg30, Xuancheng Jingrui New Materials Co., Xuancheng, China), (ii) ZnO nanoparticles with particle size < 100 nm (Sigma-Aldrich, Prague, Czech Republic) and (iii) La<sub>2</sub>O<sub>3</sub> nanoparticles with particle size < 100 nm (Sigma-Aldrich, Prague, Czech Republic). All chemicals were used without further modifications such as purification (as supplied by the manufacturer).

## 2.2. Synthesis of Latexes

Using the technique of semi-continuous emulsion radical polymerization, four series of acrylic latexes were prepared, which differed in the type and content of inorganic nanoparticles. To allow interparticle crosslinking, DAAM providing ketone carbonyl functional groups for subsequent crosslinking with a hydrazide crosslinking agent was added to the polymer chain. DAAM and nanoparticles were delivered to the system only in the second phase of the monomer drip. The ratio composition of the monomers making up all the latexes was: 86 g MMA, 106 g BA, and 8 g MAA dosed in the first phase and 78 g MMA, 104 g BA, 8 g MAA, and 10 g DAAM dosed in the second phase. The ratio of acrylic monomers forming latex particles was chosen so that the calculated glass transition temperature ( $T_g$ ) of the latex polymer was around 10 °C (calculated according to Fox's equation [86]) to ensure sufficient film formation and non-stick coatings. The  $L_0$  latex sample was a reference without the corresponding inorganic nanoparticles, while the  $L_{ZnO}$  samples contained ZnO nanoparticles, the  $L_{MgO}$  samples contained MgO nanoparticles and the  $L_{La_2O_3}$  samples contained  $La_2O_3$  nanoparticles, each with a concentration of 0.5, 1, and 1.5 wt.% (based on the total amount of monomers). The last series of  $L_{MgO+ZnO}$  acrylic latexes combined MgO and ZnO nanoparticles, with MgO nanoparticles each being supplied with a concentration of 1 wt.% and ZnO nanoparticles in a concentration of 0.25, 0.5 and 0.75 wt.% (based on the total amount of monomers).

The latexes were prepared in a glass reaction vessel under a nitrogen atmosphere at a polymerization temperature of 85 °C according to the procedure shown in Table 1. The monomer emulsion was added dropwise to the stirred reactor (approximately 2 mL/min) in two phases; a 15 min pause was allowed between the two phases. When all the emulsion was added, the system was allowed to react for another 120 min to complete the polymerization process. (The temperature of the reaction vessel was maintained at 85 °C throughout the synthetic process).

**Table 1.** Composition of the polymerization system.

Component	Reactor Feed (g)	1. Phase (g)	2. Phase (g)
Water	140.0	150.0	250.0
Disponil FES 993	1.0	14.8	14.8
Ammonium persulphate	0.8	0.8	0.8
Monomers	-	200.0	200.0
MeO nanoparticles *	-	-	2–7

\* For latexes containing MeO nanoparticles with a concentration 0.5 wt.%—2 g, 1 wt.%—4 g, 1.25 wt.%—5 g, 1.5 wt.%—6 g and 1.75 wt.%—7 g.

To prepare a series of latexes with ZnO and  $La_2O_3$  nanoparticles, respectively, the procedure involved the preparation of an aqueous suspension with nanoparticles. To prepare the nanoparticle suspension, the ZnO/ $La_2O_3$  nanoparticles were mixed with water, which was intended to prepare a monomer emulsion for the second phase. To facilitate the fragmentation of the agglomerates, dispersion was performed using a T18 digital ULTRA-TURRAX disperser (IKA Works, Staufen, Germany) at 17,000 rpm for 15 min, followed by treatment in an ultrasonic ice bath KRAINTEK K 12.F (Kraintek s.r.o., Podhájská, Slovakia) for 1 h. The prepared aqueous nanoparticle suspension was then mixed with the monomers, emulsifier, and initiator to prepare a second phase monomer emulsion, dispersed at 3000 rpm for 3 min, and immediately metered into the reactor.

To prepare a series of latexes with MgO nanoparticles, the procedure involved the preparation of a monomer suspension with nanoparticles. First, the MgO nanopowder was mixed with the MMA and BA monomers, which were intended to prepare a monomer emulsion for the second phase. To facilitate the fragmentation of the agglomerates, dispersion was performed using a T18 digital ULTRA-TURRAX disperser (IKA Works, Staufen, Germany) at 14,000 rpm for 45 min while cooling in an ice bath followed by treatment in

an ultrasonic ice bath KRAINTEK K-12.F (Kraintek s.r.o., Podhájská, Slovakia) for 45 min. The prepared monomer suspension with nanoparticles was then mixed with water, an emulsifier, initiator, and the rest of the monomers (MAA and DAAM) intended to prepare the second phase monomer emulsion, dispersed at 3000 rpm for 3 min and immediately metered into the reactor. In the case of a series of latexes with a combination of MgO and ZnO nanoparticles, the MgO nanoparticle monomer suspension and the ZnO nanoparticle aqueous suspension were prepared according to the procedures described above with the difference that half quantities of all individual components except the MeO nanoparticles were used for the preparation of both nanoparticle suspensions. In addition, the second phase drop was divided into two steps, the monomer emulsion with MgO nanoparticles was dropped in the first step followed by an immediate feeding of the monomer emulsion containing ZnO nanoparticles in the second step.

After synthesis, the solids were filtered to calculate the coagulate content, the pH of the cold latex was adjusted to 8.5 with 10% aqueous ammonia (for latexes having an initial pH below 8.5), and finally a 10% aqueous solution of ADH was added in an amount corresponding to a molar ratio of DAAM:ADH = 2:1, whereby the self-crosslinking latex binders were prepared.

All latexes were always synthesized in triplicate for each sample to ensure reliable results.

### 2.3. Characterization of Latexes

The coagulate and coarse impurity contents of the latexes were determined by sieve analysis according to CSN 64 9008; pH was measured with a Mettler Toledo FiveEasy FE20 pH-meter (Merck KGaA, Darmstadt, Germany) [87]; the minimum film-forming temperature (MFFT) was determined by using a MFFT-60 instrument (Rhopoint Instruments, East Sussex, UK) according to ISO 2115; the storage stability of latexes was tested in two storing modes: (1) at 50 °C for 2 months; (2) at 25 °C for 2 years. The evaluation was performed using the zeta potential and the particle size by the dynamic light scattering (DLS) method on a Zetasizer Nano ZS (Malvern Panalytical, Malvern, UK) [88]; the in-can antimicrobial efficiency of the liquid latexes was tested by using Preventol® Dipslides (LANXESS Deutschland GmbH, Cologne, Germany). The in-can preservation test of antimicrobial efficiency consisted of submerging the agar part of the DipSlide into the latex for 10 s, followed by incubation at 30 °C for 120 h. The result was evaluated by using standards [89].

The determination was made from each prepared latex (each latex was prepared three times) by means to ensure reliable results.

### 2.4. Preparation of Coating Films: Latex Application to the Substrate

The latexes were applied to glass panels with a size of 200 mm × 100 mm × 5 mm to test the hardness, chemical resistance, mechanical resistance (adhesion), gloss, transparency and water whitening of coating films. Mechanical (impact) resistance and corrosion resistance were tested on coating films applied to cold-rolled low-carbon steel panels (Q-Panel steel Class 11—ISO 3574 CR1, SAE 1008/1010; the chemical composition is 0.60% max Manganese, 0.15% max Carbon, 0.03% max Phosphorus and 0.035% max Sulfur) with a size of 152 mm × 102 mm × 0.8 mm. Both the glass and steel panels were cleaned thoroughly with chloroform before the tests [90]. The liquid latexes were applied to the glass/steel substrates by using a film applicator coater (bird type applicator with a constant slot width, product of Zehntner GmbH, Schwerzenbach, Switzerland). The slot width was 150 µm for application on the glass panels and 250 µm for application on the steel panels. The coating films on the panels were allowed to dry for 10 days (except for the panels intended for flash corrosion examination) in an air-conditioned room.

For determination of the antimicrobial efficiency, the presence and location of inorganic nanoparticles and real nanoparticle content in the latex films, loose films about 1 mm thick were prepared by pouring the latexes into silicone molds. The loose films were then air-dried at RT for a month and then vacuum-dried at 30 °C to constant weight. Subsequently, for antimicrobial efficiency tests the samples were sterilized on both sides using UVR-Mi

UV germicidal radiation for 20 min. For the antifungal efficiency tests, the latexes were applied also to sterile wooden squares with a size of  $5 \times 5 \text{ cm}^2$ . The latex was applied to the wooden panels with a brush in perpendicular directions in 4 layers, with a minimum drying time of 4 h between the layers; the tests themselves were performed after a drying period of 10 days.

Each test was performed in triplicate. All the coating films—on glass, steel, wood and in silicone moulds—were exposed to a temperature of  $21 \pm 2 \text{ }^\circ\text{C}$  and relative humidity of 55% in an air-conditioned room according to CSN EN 23270 prior to the tests.

### 2.5. Description of Embedded Nanoparticles: Characterization, Content and Location

Monitoring of the change in the chemical nature of the respective embedded metal oxide nanoparticles during the synthesis was performed by X-ray diffraction (XRD) on an Empyrean (PANalytical, Almelo, The Netherlands) at 40 mA and 45 kV. The instrumental setup comprised a PIXcel3D-Medipix3 surface detector with a goniometer radius of 240 mm, a scan speed =  $0.033453 \text{ }^\circ/\text{s}$  and Ni filter (to select the  $\text{Cu K}_\alpha$  wavelength) on the diffracted beam. Using Topas software (version 4.2.1, 2010, Bruker Axs, Karlsruhe, Germany), the internal standard method was used, using 10 wt.% of internal standard  $\alpha\text{-Al}_2\text{O}_3$  (NIST SRM 676a) [91]. The testing was performed on samples subjected to the simulation of polymerization carried out in the same way as in the synthesis of latexes (see Table 1), only without the content of the relevant monomers, but also on the originally supplied nanoparticles of metal oxides. The aqueous suspension thus obtained was decanted to obtain an inorganic powder, which was dried at  $80 \text{ }^\circ\text{C}$  to constant weight and analyzed.

Determination of real nanoparticle content in coating films of acrylic latexes was performed by using of an inductively coupled plasma optical emission spectrometry (ICP-OES) using an Integra 6000 (GBC Scientific Equipment, Braeside, Australia) [92]. From the values obtained, the nanoparticle content was calculated using the simplified assumption that all nanoparticles are in the coating film only in the form of the respective metal oxide. (except for  $\text{La}_2\text{O}_3$  based, where  $\text{La}_2\text{O}_2\text{CO}_3$  was considered according to XRD analysis results).

The presence and location of inorganic nanoparticles on the surface of the latex coating films were evaluated employing an atomic force microscopy (AFM). The measurement was done applying AFM Dimension Icon (Bruker, Billerica, MA, USA) in PeakForce quantitative nanoscale mechanical mode using ScanAsyst-Air tips ( $k = 0.4 \text{ N}\cdot\text{m}^{-1}$ ). The topography and mechanical behavior of the film surface were simultaneously monitored at a scanning frequency of 0.5 Hz with a resolution of  $512 \times 512$  pixels at the area  $5 \times 5 \text{ }\mu\text{m}^2$  in a similar way as in [55]. The presence and distribution of inorganic nanoparticles inside the latex coatings was observed by means of scanning electron microscopy (SEM) using a LYRA 3 scanning electron microscope (Tescan, Brno, Czech Republic). The cryo-fractures of the polymer films were covered with a 20 nm carbon layer and measured at an accelerating voltage of 5 kV.

The change in the morphology of the nanoparticles before and after their exposure to the polymerization conditions was also monitored by SEM, by the same method of preparation as for XRD. The nanoparticles were gilded with 18 nm Au layer and measured at an accelerated voltage of 10 kV.

The determination was made from each prepared latex (each latex was prepared three times) to ensure reliable results.

### 2.6. Coating Film Property Assessment

The degree of crosslinking of acrylic latexes was evaluated based on gel content and crosslink density. The gel content was determined according to CSN EN ISO 6427 by extraction in a Soxhlet extractor with tetrahydrofuran for 24 h. Crosslinking density was performed by swelling loose films of acrylic latexes in toluene at  $35 \text{ }^\circ\text{C}$  for 7 days. The sample was then withdrawn, quickly dried with gauze and weighed to obtain the weight of the swollen sample. Equations (1)–(4), employing the theory of Flory and Rehner [93],

were used to calculate the crosslink density (expressed as moles of crosslinks per cm<sup>3</sup> of polymer network), as given in the following:

$$M_c = \frac{V_1 \rho_p [\phi^{1/3} - \phi/2]}{-[\ln(1 - \phi) + \phi + \chi \phi^2]} \quad (1)$$

$$\phi = \frac{W_p \rho_s}{W_p \rho_s + W_s \rho_p} \quad (2)$$

$$\chi = 0.34 + \frac{V_1}{RT} (\delta_1 - \delta_2)^2 \quad (3)$$

$$\text{Crosslink density} = \frac{\rho_p}{M_c} \quad (4)$$

where the abbreviations indicate:  $M_c$ —average molecular weight between crosslinking;  $V_1$ —molar volume of toluene (106.3 cm<sup>3</sup>/mol);  $\rho_p$ —density of polymer that was calculated to be 1.11 g/cm<sup>3</sup> for the BA/MMA/MAA (53/43/4 by weight) copolymer from 1.06, 1.18 and 1.015 g/cm<sup>3</sup> for poly(BA), poly(MMA) and poly(MAA), respectively;  $\phi$ —volume fraction of the gel polymer in the swollen gel;  $W_p$  and  $W_s$  are the weight fractions of the gel polymer and solvent (toluene) in the swollen gel, respectively;  $\rho_s$ —density of solvent (0.8669 g/cm<sup>3</sup>);  $\chi$ —polymer and solvent interaction parameter;  $\delta_1$ —solubility parameter of polymer that was calculated to be 9.16 (cal/cm<sup>3</sup>)<sup>1/2</sup> for the BA/MMA/MAA (53/43/4 by weight) copolymer from 9.0, 9.3 and 9.8 (cal/cm<sup>3</sup>)<sup>1/2</sup> for poly(BA), poly(MMA) and poly(MAA), respectively; and  $\delta_2$ —solubility parameter of toluene, 8.9 (cal/cm<sup>3</sup>)<sup>1/2</sup> [94,95].

The optical properties of coating films were evaluated with respect to gloss, transparency and water whitening. The gloss was evaluated according to CSN EN ISO 2813 (using a gloss-measuring geometry at 20°). Since these are transparent coatings, the glass panels on which the measurement was performed were sprayed with black matte paint (RAL 9005) and the measurement was determined by a micro TRI-gloss  $\mu$  instrument (BYK-Gardner, Wesel, Germany). The transparency and water whitening of coating films were evaluated by light transmission (transmittance measurement at a wavelength of 500 nm) using a ColorQuest XE Spectrometer (Hunterlab, Reston, VA, USA). Initially, transparency measurements were performed and then the coating films were exposed to distilled water for 48 h at room temperature, then measurements were immediately performed on the exposed areas of the coating film. The degree of water whitening— $W$  in % was calculated by  $W = 100(T_0 - T_t)/T_0$ , where the abbreviations indicate:  $T_0$ —the transmittance of sample before distilled water exposure and  $T_t$ —the transmittance of sample after performing the immersion test.

The hardness of the coating films was evaluated according to CSN EN ISO 1522—Paints and varnishes—Pendulum damping test; Persoz type pendulum (3034M001 pendulum, Elcometer Instruments GmbH, Aalen, Germany). The mechanical properties (mechanical resistance) of the coating films were assessed according to CSN EN ISO 6272-2—Paints and varnishes—Rapid-deformation (impact resistance) test using an Elcometer 1615 variable impact tester (Elcometer Instruments GmbH, Aalen, Germany) with a steel falling weight of 1000 g with 20 ± 1 mm hemispherical end. Tests according to CSN ISO 2409, the cross-cut test, were also made. An Elcometer cross-cut system (Elcometer Instruments GmbH, Aalen, Germany) with 6 parallel knives 1 mm apart was used. After making the grid, the damage was visually assessed according to a classification scale from 0 to 5, where 0 indicates the best result (Table S1, see Supplementary Materials). Chemical resistance of the coating films was assessed according to ASTM D-4752-10—rubbing test with methyl ethyl ketone (MEK).

Flash corrosion resistance of the coating films was evaluated after the coating was applied to the steel substrate and assessed through a laboratory test to identify any flash corrosion [64]. The laboratory test was made on coating films deposited on steel panels which, after drying at 21 ± 2 °C, RH 50 ± 5% for 2 h, were stored in a refrigerator at 5 °C

for 16 h. After removal from the refrigerator, the entire coating film was uniformly covered with a filter paper that was pre-wetted with distilled water, and the system was covered with a heavy glass plate to achieve close contact of the coating film with the water. The water was allowed to act for 2 h at room temperature. Then the filter paper was removed, the coating film was dried, and corrosion phenomena were scored as per ASTM D 610-85; coloration was scored using Gardner's iodometric scale (see Table S2) [63].

All coating film evaluation tests were always performed in triplicate for each sample to ensure reliable results.

### 2.7. Testing of Antimicrobial Efficiency of Coating Films

The antimicrobial efficiency of the coating films was evaluated using a modified method ISO 22196 [96] to determine the antibacterial activity. Based on this modified method, the most effective concentration of the given nanoparticles was selected for each series and was subsequently tested using the ISO 22196 method. For these selected samples, their antifungal efficiency of coating films on a wooden substrate was further determined using a modified method ASTM D5590 [97]. Four bacterial strains were used for antimicrobial tests, namely *Staphylococcus aureus* (*S. aureus*, CCM 4516), *Escherichia coli* (*E. coli*, CCM 4517), *Enterococcus faecalis* (*E. faecalis*, CCM 3956) and *Klebsiella pneumoniae* (*K. pneumoniae*, CCM 4425) and two fungal strains, namely *Penicillium chrysogenum* (*P. chrysogenum*, CCM 8034) and *Aspergillus brasiliensis* (*A. brasiliensis*, CCM 8222). All the microbial strains were provided by the Czech Collection of Microorganisms (Masaryk University, Brno, Czech Republic).

The testing of antibacterial activity according to ISO 22196 method and the modified ISO 22196 method was performed on sterile loose films with dimensions of  $25 \times 25 \text{ mm}^2$  which were inoculated with 0.1 mL of a specific standardized bacterial suspension (24 h culture), namely *S. aureus* ( $7.4 \times 10^6 \text{ cfu/mL}$ ), *E. coli* ( $6.9 \times 10^6 \text{ cfu/mL}$ ), *E. faecalis* ( $6.1 \times 10^6 \text{ cfu/mL}$ ) and *K. pneumoniae* ( $5.8 \times 10^6 \text{ cfu/mL}$ ). The inoculated samples were then covered with a sterile polypropylene film (sterilized with 70% ethanol) with a size of  $20 \times 20 \text{ mm}^2$ . Then the samples were incubated at  $35 \text{ }^\circ\text{C}$  for 24 h at 95% RH. In the case of the modified ISO 22196, the samples were imprinted on a Plate Count Agar (HIMEDIA, Mumbai, India) after the removal of the polypropylene film. Each sample was imprinted on three different agar areas (see Figure S1) and incubated at  $35 \text{ }^\circ\text{C}$  for 24 h. The results were then evaluated from 0 to 5, with 0 representing the best antibacterial activity, i.e., without the growth of bacterial colonies.

If the ISO 22196 method was followed, after removing the polypropylene film, the samples were rinsed with 2.5 mL of SCDLP flushing solution (Lach-ner a.s., Neratovic, Czech Republic) and a dilution series from 0 to  $10^{-7}$  was prepared from the thus prepared microbial suspension. From the dilution series prepared in this way, 1 mL was always taken, which was placed in a Petri dish and filled with  $45 \text{ }^\circ\text{C}$  warm MPA nutrient agar No. 2 (HIMEDIA, India), and the whole system was mixed and incubated at  $35 \text{ }^\circ\text{C}$ . After a 24 h incubation, bacterial contamination readings were performed (for dilutions with 30–300 bacterial colonies). The arithmetic mean was calculated from the obtained values and a conversion was carried out according to the Equations (5) and (6):

$$N = (100 \times C \times D \times V) / A \quad (5)$$

$$R = U_t - A_t \quad (6)$$

where N is the number of viable bacteria per  $\text{cm}^2$  of test sample; R is antimicrobial activity; C is the average number of bacteria; D is the dilution value; V is the volume of rinsing solution added to the sample; A is the surface area of the cover foil in  $\text{mm}^2$ ;  $U_t$  is the average value of the logarithm of viable bacteria in units of cells/ $\text{cm}^2$  of untreated test samples after 24 h of incubation; and  $A_t$  is the average value of the logarithm of viable bacteria in units of cells/ $\text{cm}^2$  of test specimens after 24 h of incubation.

Testing of antifungal activity was performed on sterile  $40 \times 40 \text{ mm}^2$  wooden panels treated with the coating film. The 5-day cultures were suspended in physiological saline solution with 0.005% (*w/v*) of TWEEN<sup>®</sup> 20 (Sigma-Aldrich, Prague, Czech Republic). Specifically standardized fungal suspensions were used, namely *P. chrysogenum* ( $2.4 \times 10^6$  spores/mL) and *A. brasiliensis* ( $3.1 \times 10^6$  spores/mL). Sterile samples placed in the center of a Petri dish with MALT agar (HIMEDIA, Mumbai, India) were inoculated with 0.1 mL of the appropriate fungal suspension, which was evenly distributed (with an L-shaped hockey stick) over the entire surface. The samples thus prepared were incubated at  $25 \pm 2 \text{ }^\circ\text{C}$  and 90% RH for 28 days. The results were then evaluated by standard specification from 0 to 4, with 0 representing the best antifungal activity, i.e., without the growth of mould.

All antimicrobial tests were always performed in triplicate for each sample to ensure reliable results of the antimicrobial efficacy.

### 3. Results and Discussion

#### 3.1. Properties of Latexes

Characteristic properties of all prepared liquid latexes are given in Table 2. As can be seen from the results, the resulting properties of the latexes were affected by both the type of added nanoparticles and their concentration. As already reported in previously published papers [55,56,98], it was found for all series of latexes that the coagulum content increased with the increasing content of incorporated inorganic nanoparticles. From this it can be concluded that the presence of nanostructured MeO caused a slight decrease in the colloidal stability of the dispersion during synthesis, probably due to the hydration reaction of the respective metal oxide to form water-insoluble relevant hydroxide and dissociated  $\text{OH}^-$  and  $\text{Me}^{x+}$  ions, which resulted in increased ionic strength of the dispersion medium, i.e., agglomeration of latex particles. The presence of dissociated ions (probably in a low concentration, but not negligible) is also evidenced by the increased pH value, which again increased with the increasing concentration of nanoparticles. When comparing the types of nanoparticles, the pH value is the highest in the case of latexes containing MgO nanoparticles, which corresponds to their solubility in water compared to nanoparticles ZnO and  $\text{La}_2\text{O}_3$  (solubility in water at room temperature:  $\text{MgO} = 86 \text{ mg/L}$ ,  $\text{ZnO} = 1.6 \text{ mg/L}$  and  $\text{La}_2\text{O}_3 = 4 \text{ mg/L}$  [99]).

**Table 2.** Characteristics of latexes differing in type and content of embedded nanoparticles.

Sample	Theoretical Nanoparticle Content (wt.%)		Coagulum Content (wt.%) <sup>1,2</sup>	pH <sup>1</sup>	MFFT ( $^\circ\text{C}$ ) <sup>3</sup>	In-Can Stability <sup>3</sup>	
	Coating Film	Liquid Binder				Bacteria (cfu/mL)	Fungi (deg.)
L <sub>0</sub>	0	0	0.1	$2.12 \pm 0.21$	$8.1 \pm 0.2$	$1 \times 10^6$	Heavy
L <sub>MgO-0.5%</sub>	0.5	0.2	0.3	$7.50 \pm 0.16$	$3.0 \pm 0.1$	$1 \times 10^5$	Heavy
L <sub>MgO-1%</sub>	1	0.4	0.5	$8.62 \pm 0.21$	$2.2 \pm 0.2$	$1 \times 10^4$	Moderate
L <sub>MgO-1.5%</sub>	1.5	0.6	0.6	$10.24 \pm 0.32$	$0.5 \pm 0.2$	<1000	None
L <sub>ZnO-0.5%</sub>	0.5	0.2	0.4	$5.53 \pm 0.19$	$9.0 \pm 0.3$	<1000	None
L <sub>ZnO-1%</sub>	1	0.4	0.5	$6.00 \pm 0.13$	$9.9 \pm 0.4$	<1000	None
L <sub>ZnO-1.5%</sub>	1.5	0.6	0.8	$6.08 \pm 0.16$	$11.5 \pm 0.4$	<1000	None
L <sub>MgO+ZnO-1.25%</sub>	1.25	0.5	1.1	$10.12 \pm 0.28$	$2.5 \pm 0.2$	<1000	None
L <sub>MgO+ZnO-1.5%</sub>	1.5	0.6	1.9	$9.93 \pm 0.17$	$4.8 \pm 0.2$	<1000	None
L <sub>MgO+ZnO-1.75%</sub>	1.75	0.7	2.8	$9.46 \pm 0.15$	$6.9 \pm 0.4$	<1000	None
L <sub>La2O3-0.5%</sub>	0.5	0.2	0.3	$5.27 \pm 0.11$	$10.7 \pm 0.3$	$1 \times 10^4$	Moderate
L <sub>La2O3-1%</sub>	1	0.4	0.6	$5.71 \pm 0.09$	$11.9 \pm 0.2$	1000	Light
L <sub>La2O3-1.5%</sub>	1.5	0.6	1.0	$5.85 \pm 0.16$	$14.4 \pm 0.3$	<1000	None

<sup>1</sup> Determined before ammonia and ADH addition to the latex. <sup>2</sup> Standard deviations did not exceed 0.05%.

<sup>3</sup> Determined after ammonia and ADH addition to the latex.

The effect of the type and concentration of embedded nanoparticles on MFFT was also observed, where the results probably indicate two phenomena caused by the presence of nanoparticles, namely interfacial ionic crosslinking owing to the presence of dissociated  $\text{Me}^{x+}$  ions leading to increased MFFT and hydroplasticization of carboxyl emulsion copolymer leading to decreased MFFT. The first effect was more pronounced in latexes containing ZnO and  $\text{La}_2\text{O}_3$  nanoparticles, which exhibited increased MFFT with increasing concentration of nanoparticles, i.e., with increasing concentration of dissociated  $\text{Me}^{x+}$  ions leading to ion-phase crosslinked film through the reaction between carboxyl groups of emulsion copolymer and metal cations [55,56]. This led to suppression of mobility and inter-diffusion of the polymer chains, thereby the deformability of the latex particles in the coalescence phase became worse, leading to an increase in MFFT. In contrast, for the latexes with MgO nanoparticles, a second effect causing a decrease in MFFT with increasing nanoparticle concentration was observed more markedly, apparently due to hydroplasticization of the carboxyl emulsion copolymer. The solubility of MgO in the aqueous dispersion medium, causing the pH to increase, as described above, caused a permanent neutralization of a significant amount of carboxyl groups during film formation. The ionized carboxyl groups are responsible for the higher amount of molecularly bound water in the latex copolymer [100,101], which results in softening of the polymer chains throughout the film drying process, leading to a decrease in MFFT even with dense interfacial crosslinking. Significant hydroplasticization of latex particles was also observed in latexes combining MgO and ZnO nanoparticles, which, however, decreased with increasing concentration of ZnO nanoparticles (concentration of incorporated MgO nanoparticles was set constant—theoretically 1 wt.% in the coating). This effect was probably due to decreasing the real content of MgO nanoparticles in the latex due to intensified coagulum formation rich in MeO nanoparticles.

The results of in-can testing of aqueous dispersions provided evidence of the antimicrobial efficacy of dispersed MeO nanoparticles. While the reference latex (nanoparticle-free) showed the presence of bacteria at a density of  $1 \times 10^6$  cfu/mL and high yeast coverage, the latexes with nanoparticles showed suppression of the growth of microorganisms. Based on the results, ZnO nanoparticles, which already showed microbicidal activity at the lowest concentration, appeared to be the most suitable in-can antimicrobial additive. In contrast, MgO and  $\text{La}_2\text{O}_3$  nanoparticles showed microbicidal activity only at the highest concentration, and at lower concentrations of nanoparticles, there was only a partial suppression of the growth of microorganisms, which increased with increasing nanoparticle concentration. However, a serious disadvantage of ZnO nanoparticles is their toxicity to the aquatic environment [78,79] and mammalian cells [80–83]. It is, therefore, appropriate to decrease the concentration of ZnO nanoparticles as low as possible and look for new alternatives to antimicrobial protection. For this reason, a series of latexes combining ZnO and MgO nanoparticles was also prepared, where antimicrobial protection of the liquid latex occurred at a theoretical concentration of 0.25 and 1 wt.% of ZnO and MgO nanoparticles, respectively. The antimicrobial activity of MeO nanoparticles can be attributed to lipid peroxidation, the formation of reactive oxygen species or the presence of metal cations destroying MO enzymes. However, it should be noted here that the exact mechanism of antimicrobial protection of MeO nanoparticles has not yet been fully elucidated. Alkaline latexes may also play a role in their alkalinity, which creates an unfavorable environment for MOs and also increases the activity of reactive oxygen species [83].

In view of the risk of premature destabilization of the latexes during storage due to the presence of inorganic nanoparticles, testing of the stability of the latexes during storage was performed. Particle size and zeta potential were assessed before storage (the same day of synthesis) and after storage: (i) after 2 months at 50 °C and (ii) after 2 years at RT. The measurement results are shown in Table 3. It is clear from the results that the size of latex particles was significantly affected only in the case of latexes containing MgO nanoparticles, where the particle size was increased with increasing MgO concentration, probably due to the so-called alkali-swelling effect [102]. In the case of zeta potential, the initial values were found to decrease with increasing nanoparticle concentration, which

was most pronounced for latexes containing MgO nanoparticles, probably owing to the increased ionic strength of the dispersion medium due to the dissolution of the respective MeO. Latexes containing a theoretical concentration of  $\geq 1$ wt.% of MgO showed values close to  $-30$  mV, indicating an initial risk of instability. Despite this fact, all these latexes have been shown to be stable during storage and resistant to aggregation. After testing, no obvious coagulation, no sedimentation, and no significant changes in the tested properties were observed in any latex. Based on these results, it can be concluded that all latexes can be considered long-term stable. To monitor the effect of the MeO nanoparticle type on zeta potential, the individual zeta potential distribution curves for latexes (tested on the same day of synthesis) with the highest concentration of nanoparticles were shown in Figure S2.

**Table 3.** Results of storage stability testing.

Sample	Same Day of Synthesis		After Storage Test		After 2 Years at RT	
	Particle Size (nm)	Zeta Potential (mV)	Particle Size (nm)	Zeta Potential (mV)	Particle Size (nm)	Zeta Potential (mV)
L <sub>0</sub>	125.5 ± 2.0	−39.0 ± 1.7	126.3 ± 3.7	−37.0 ± 1.3	123.7 ± 2.8	−38.2 ± 1.3
L <sub>MgO-0.5%</sub>	130.5 ± 1.2	−34.7 ± 0.9	131.7 ± 2.6	−34.8 ± 0.5	131.6 ± 2.2	−34.2 ± 1.1
L <sub>MgO-1%</sub>	152.4 ± 2.6	−28.5 ± 1.4	151.2 ± 1.8	−26.5 ± 1.2	151.6 ± 1.8	−25.0 ± 0.6
L <sub>MgO-1.5%</sub>	206.8 ± 3.5	−26.8 ± 0.8	205.7 ± 3.6	−25.0 ± 0.7	200.7 ± 3.6	−24.3 ± 0.5
L <sub>ZnO-0.5%</sub>	113.3 ± 1.3	−37.5 ± 0.6	116.1 ± 2.0	−38.9 ± 0.8	115.6 ± 3.9	−41.1 ± 1.1
L <sub>ZnO-1%</sub>	121.9 ± 2.9	−32.4 ± 0.4	122.5 ± 2.0	−36.7 ± 1.1	126.5 ± 1.6	−43.2 ± 1.4
L <sub>ZnO-1.5%</sub>	123.9 ± 2.8	−31.7 ± 0.3	126.1 ± 1.9	−34.5 ± 0.6	128.1 ± 1.4	−45.1 ± 1.1
L <sub>MgO+ZnO-1.25%</sub>	161.0 ± 3.5	−29.7 ± 1.3	159.4 ± 2.4	−25.1 ± 0.3	162.5 ± 1.6	−25.4 ± 1.2
L <sub>MgO+ZnO-1.5%</sub>	147.3 ± 2.9	−29.1 ± 1.2	148.8 ± 3.4	−22.9 ± 0.9	152.5 ± 2.9	−23.5 ± 1.0
L <sub>MgO+ZnO-1.75%</sub>	140.1 ± 1.8	−26.1 ± 1.0	138.7 ± 1.7	−21.5 ± 0.7	141.2 ± 2.4	−23.5 ± 1.0
L <sub>La2O3-0.5%</sub>	92.7 ± 0.7	−47.1 ± 1.4	92.1 ± 1.2	−42.4 ± 1.4	92.7 ± 1.1	−44.3 ± 1.5
L <sub>La2O3-1%</sub>	117.7 ± 1.4	−43.8 ± 0.8	117.1 ± 0.6	−39.3 ± 1.6	117.8 ± 1.0	−43.3 ± 1.0
L <sub>La2O3-1.5%</sub>	119.3 ± 1.7	−39.0 ± 0.8	118.6 ± 1.1	−35.2 ± 1.2	119.0 ± 1.5	−38.0 ± 1.4

### 3.2. Embedded Nanoparticles: Characterization, Real Content, and Location

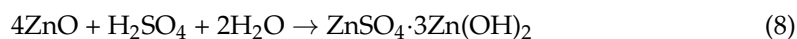
Because the surface untreated inorganic MeO nanoparticles were inserted during latex synthesis, it was considered that they may be chemically transformed during this process. To determine the chemical nature of transformed nanoparticles, a simulation of the effect of polymerization conditions and reactants was performed without the presence of monomers in the reaction system, followed by isolation of nanoparticles from the aqueous environment by decantation and air-drying. (For this reason, a significant amount of dissolved compounds from the original MeOs was probably removed and the identified chemical nature of nanoparticles, therefore, does not fully correspond to the real nanoparticles in the latex coating film.) Subsequently, the chemical structure of the original inorganic nanoparticles and those subjected to polymerization simulation were compared by XRD, as shown in Table 4 and in Figures S3–S5.

**Table 4.** Chemical nature of nanoparticles before and after exposure to polymerization conditions detected by XRD.

Nanoparticle Type	Original State (wt.%)				Final State (wt.%)			
	Oxide	Hydroxide	Sulfate	Dioxy carbonate	Oxide	Hydroxide	Sulfate	Dioxy carbonate
MgO	82.6 ± 0.8	17.3 ± 0.4	~0	~0	~0	96.7 ± 0.9	3.3 ± 0.2	~0
ZnO	96.4 ± 0.9	3.6 ± 0.2	~0	~0	34.0 ± 0.4	45.3 ± 0.5	20.7 ± 0.3	~0
La <sub>2</sub> O <sub>3</sub>	~0	~0	~0	100	~0	~0	~0	100

The results showed that MgO nanoparticles, which were in the original state of periclase (MgO) with a small admixture of brucite (Mg(OH)<sub>2</sub>), converted almost exclusively

to brucite after synthesis. The conversion of MgO to Mg(OH)<sub>2</sub> is shown by Equation (7). The original chemical structure of nanoparticulate ZnO was zincite (amorphous ZnO), which after synthesis was largely converted to zinc sulfate hydroxide (ZnSO<sub>4</sub>·3Zn(OH)<sub>2</sub>). The conversion of ZnO to ZnSO<sub>4</sub>·3Zn(OH)<sub>2</sub> is shown by Equation (8). In the systems combining MgO and ZnO nanoparticles, the conversion of inorganic nanoparticles probably takes place in the same way as in the case of inserting separate MgO or ZnO nanoparticles. The original chemical structure of La<sub>2</sub>O<sub>3</sub> nanoparticles was lanthanum dioxycarbonate (La<sub>2</sub>O<sub>2</sub>CO<sub>3</sub>), which is in line with the literature [103,104], as lanthanum oxide is known to be very sensitive to water and carbon dioxide, so its exposure to these conditions (i.e., including ambient air) leads to hydroxylation and/or carbonization [103,105]. The conversion of La<sub>2</sub>O<sub>3</sub> to La<sub>2</sub>O<sub>2</sub>CO<sub>3</sub> is shown by Equation (9). The results revealed that in the case of La<sub>2</sub>O<sub>3</sub>-based nanoparticles, no transformation occurred due to synthesis. The nanoparticles were in the form of La<sub>2</sub>O<sub>2</sub>CO<sub>3</sub> both before and after synthesis.



The effect of polymerization conditions on the morphology of nanoparticles was also monitored by SEM, the measurement being performed before latex synthesis (as supplied by the manufacturer) and after subjecting the nanoparticles to the simulation of the effect of polymerization conditions. As can be observed in Figure 3, all types of nanoparticles were agglomerates, with the size of the primary particles differing with respect to the type of nanoparticles. The ZnO and MgO nanoparticles were mainly spherical primary particles with a size of 30–60 and 100–200 nm for ZnO and MgO, respectively. In contrast, La<sub>2</sub>O<sub>3</sub> nanoparticles had the character of a porous network (perforated cheese) without distinct primary particles with a length of up to several μm and a depth in units of nm. After exposure to the polymerization conditions, a slight increase in the size of the primary particles was observed in the case of ZnO, probably due to the hydration of the nanoparticle surface with a layer of ZnSO<sub>4</sub>·3Zn(OH)<sub>2</sub>. For MgO, the change in particle shape from spherical to lamellar was observed, which is a typical morphology of nanostructured Mg(OH)<sub>2</sub> [106]. No significant change in particle morphology was observed for La<sub>2</sub>O<sub>3</sub>-based nanoparticles.

The content of embedded nanoparticles in coating films was determined using ICP-OES and was used to calculate the real content of nanoparticles in the coating film. The analysis showed that the incorporation efficiency of nanoparticles, both dissolved and stably dispersed in the aqueous latex medium, decreased with increasing content of inorganic nanoparticles incorporated into the latex (see Table 5), which also indicates an increase in the proportion of inorganic nanoparticles trapped in the coagulum (see Table 2). For this reason, further efforts to increase the content of incorporated nanoparticles seem inefficient.

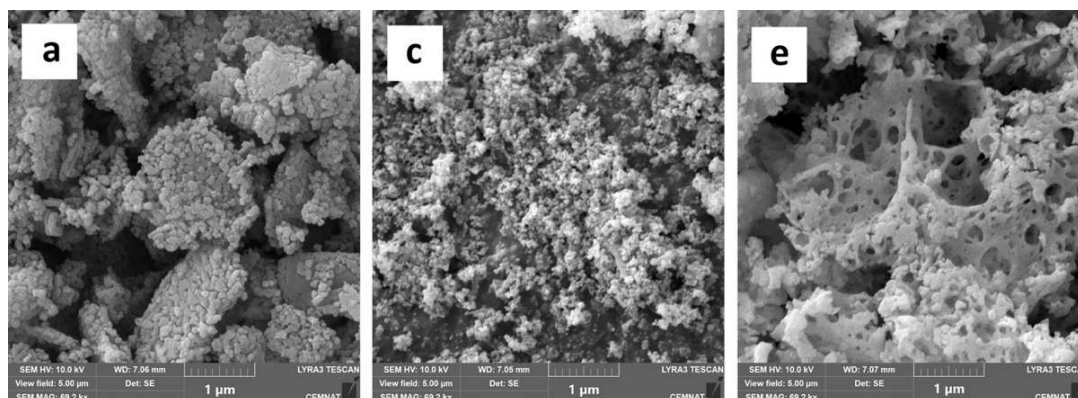
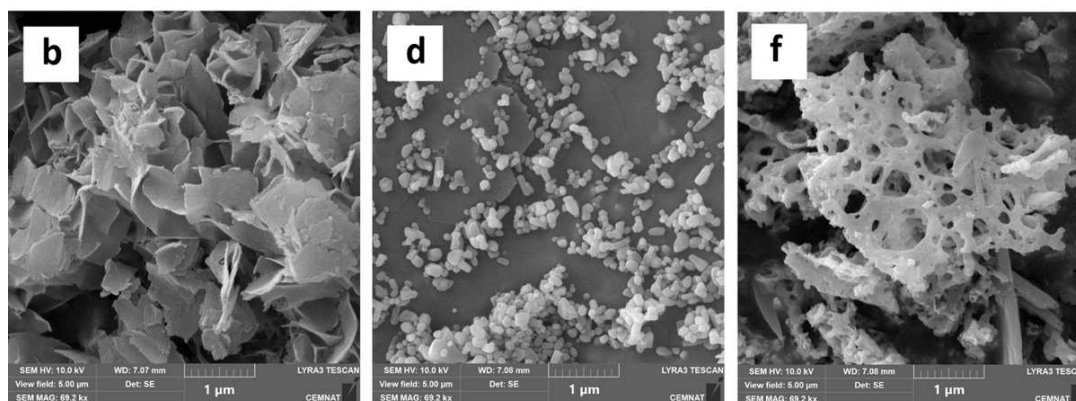


Figure 3. Cont.



**Figure 3.** SEM photographs of nanoparticles before and after latex synthesis: MgO-based nanoparticles ((a)-before, (b)-after); ZnO-based nanoparticles ((c)-before, (d)-after) and La<sub>2</sub>O<sub>3</sub>-based nanoparticles ((e)-before, (f)-after).

**Table 5.** Real nanoparticle content in coating films and aqueous dispersions.

Type of Nano-Particles	Sample	Theoretical Concentration of Nanoparticles in Coating Film (wt.%)	Metal Concentration (mg/kg)	Real Concentration of Nanoparticles in Coating Film (wt.%) <sup>2</sup>	Real Concentration of Nanoparticles in Liquid Latex (wt.%) <sup>3</sup>
		L <sub>0</sub>	0	0	0
Mg	L <sub>MgO</sub> -0.5%	0.5	2948 ± 29	0.49	0.20
	L <sub>MgO</sub> -1%	1	5561 ± 23	0.92	0.36
	L <sub>MgO</sub> -1.5%	1.5	7900 ± 41	1.31	0.52
Zn	L <sub>ZnO</sub> -0.5%	0.5	3561 ± 34	0.44	0.18
	L <sub>ZnO</sub> -1%	1	7288 ± 47	0.91	0.36
	L <sub>ZnO</sub> -1.5%	1.5	10,618 ± 31	1.32	0.53
Mg + Zn	L <sub>MgO+ZnO</sub> -1.25%	1 + 0.25 <sup>1</sup>	5548 ± 41 + 1728 ± 19	0.92 + 0.22	0.37 + 0.09
	L <sub>MgO+ZnO</sub> -1.5%	1 + 0.5 <sup>1</sup>	5478 ± 37 + 3158 ± 27	0.91 + 0.39	0.36 + 0.16
	L <sub>MgO+ZnO</sub> -1.75%	1 + 0.75 <sup>1</sup>	5198 ± 34 + 4209 ± 38	0.86 + 0.52	0.34 + 0.21
La	L <sub>La2O3</sub> -0.5%	0.5	3683 ± 26	0.49	0.20
	L <sub>La2O3</sub> -1%	1	7004 ± 35	0.93	0.37
	L <sub>La2O3</sub> -1.5%	1.5	10,580 ± 31	1.41	0.56

<sup>1</sup> Latexes combining nanoparticles MgO and ZnO were always prepared using constant amount of MgO (1 wt.% with respect to monomers) and varying amount of ZnO (0.25, 0.5 and 0.75 wt.% with respect to monomers) to achieve the desired concentration. <sup>2</sup> The percentage of inorganic nanoparticles in the dried coating film from the ICP-OES results was calculated using the simplified assumption that the determined metal (Mg and Zn) in the polymer film was only in the form of the corresponding oxide and La was present in the form of dioxycarbonate (as determined by XRD). <sup>3</sup> The percentage of inorganic nanoparticles in the liquid latex was calculated from the actual concentration of nanoparticles in the coating film and the dry matter of the respective latex.

The presence and location of MeO nanoparticles on the surface of the dried polymer matrix were investigated by AFM. The topography and mechanical behavior were always compared for the highest concentration of MeO nanoparticles used for each series (i.e., L<sub>MgO</sub>-1.5%, L<sub>ZnO</sub>-1.5%, L<sub>MgO+ZnO</sub>-1.75%, and L<sub>La2O3</sub>-1.5%) and latex without nanoparticles L<sub>0</sub> (see Figure 4). The AFM results show that the surface of the L<sub>0</sub> (blank) showed a hexagonal structure and a homogeneous mechanical map of coalesced polymer particles in the dried coating film (see Figure 4a,b). The addition of any MeO nanoparticles used led to a partial loss of hexagonal structure and loss of homogeneity in mechanical behavior, as the nanoparticles used are inorganic with a significantly stiffer character compared to polymer particles [107]. MeO nanoparticles were detected as topographically elevated (brighter dots in the left column) and stiffer (white dots in the right column). The mechanical response is more contrasting compared to the topography due to the partial immersion of the MeO nanoparticles in the polymer film caused by the surface tension during the drying

process. All types of MeO particles were well separated, meeting the nano-size requirement ( $<100$  nm) in all three scanned areas. The MgO nanoparticles had a lamellar shape with a thickness  $<50$  nm and a length  $>500$  nm (see arrows in Figure 4d). ZnO nanoparticles were detected as spherical particles with a lateral size of 80 nm homogeneously distributed over the surface (see arrows in Figure 4f). The film sample with a mixture of MgO and ZnO showed a different behavior of partially agglomerated spherical particles (probably ZnO) in the middle of the so-called snowflake with a lamellar character of the tails (MgO lamellae), see Figure 4 h. The surface of the sample with  $\text{La}_2\text{O}_3$  nanoparticles was rough compared to the other samples and therefore the particles are not clearly visible (see Figure 4i) but using mechanical behavior in the log module showed that  $\text{La}_2\text{O}_3$  nanoparticles were well-dispersed particles with an average size of 100 nm (see arrows in Figure 4j). Further, AFM images in three-dimensional (3D) form and root mean square (RMS) parameters (see Figure S6 and Table S3, respectively) were used for sample roughness evaluation [108,109].

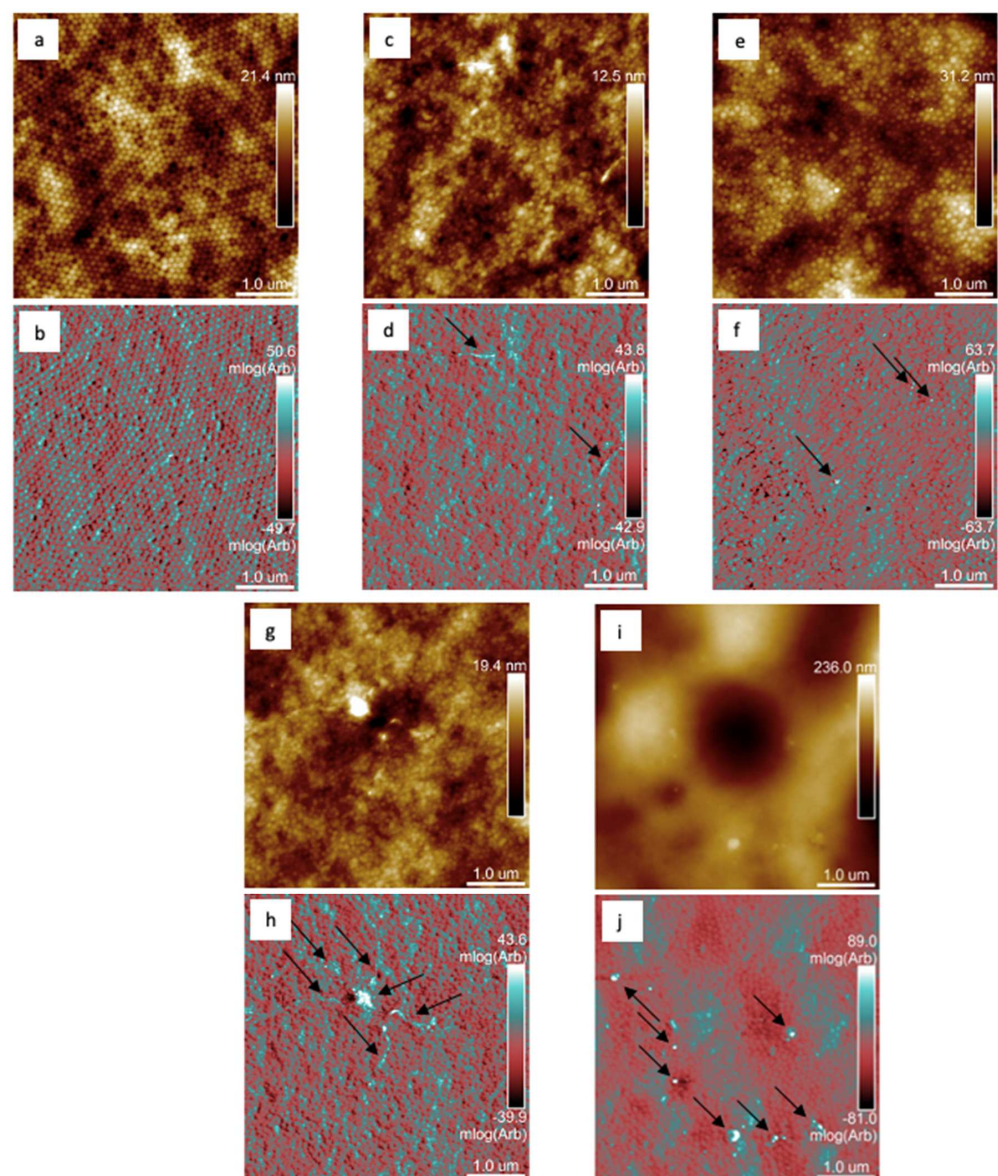


**Figure 4.** AFM scans of the topography (brown images—the upper half of the column) and mechanical behavior (in the log of modulus, blue–red images—the lower half of the column): for blank sample  $L_0$  (a,b), sample  $L_{\text{MgO}-1.5\%}$  containing MgO-based nanoparticles (c,d), sample  $L_{\text{ZnO}-1.5\%}$  containing ZnO-based nanoparticles (e,f), sample  $L_{\text{MgO}+\text{ZnO}-1.75\%}$  containing MgO-based and ZnO-based nanoparticles (g,h), and sample  $L_{\text{La}_2\text{O}_3-1.5\%}$  containing  $\text{La}_2\text{O}_3$ -based nanoparticles (i,j).

The morphology and distribution of MeO nanoparticles inside the dried latex films were investigated by SEM. SEM photomicrographs were taken in both secondary electron (SE) mode (demonstrating topographic view) and backscattered electron (BSE) mode (representing elementary surface contrast). As shown in Figure 5, the dried polymeric materials did not contain any micro-large inorganic agglomerates, except for the combination of MgO and ZnO nanoparticles, which formed the so-called snowflakes, as described above. In other cases, the embedded MeOs were in the form of primary nanoparticles that were regularly distributed inside a polymer matrix, which is a favourable condition for the transparency of the final coatings.

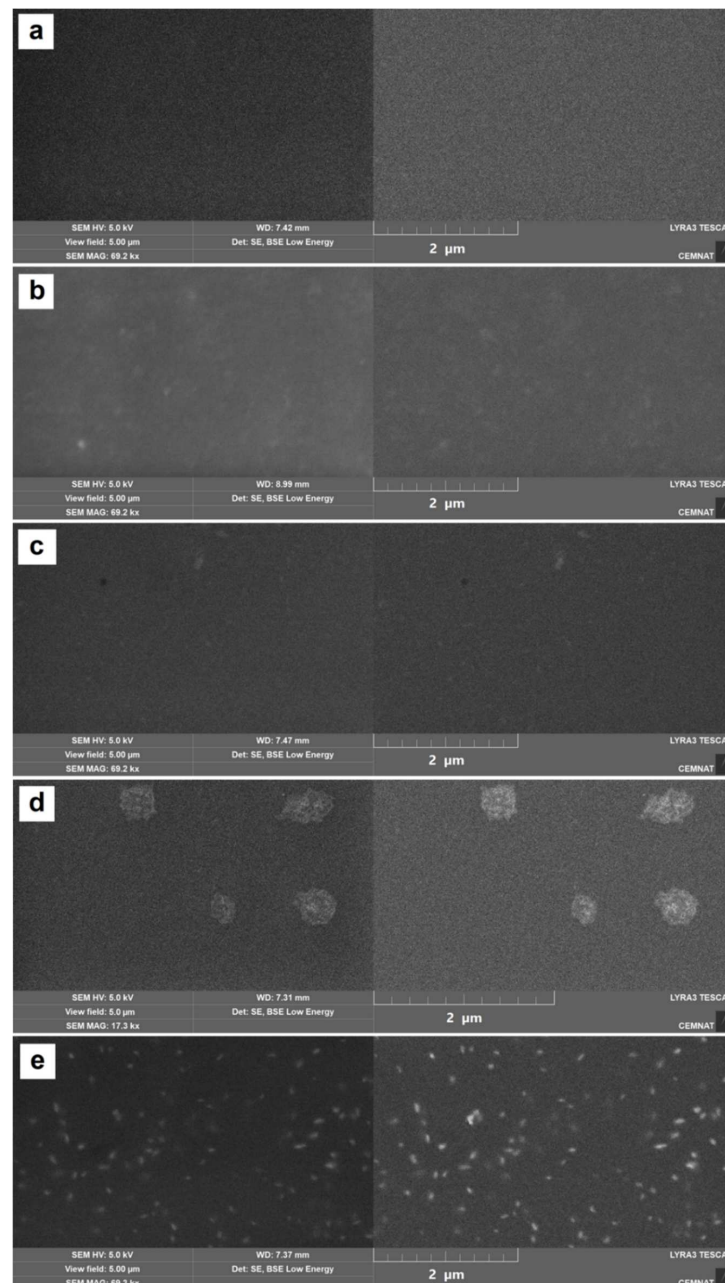


**Figure 5.** SEM photographs of cryofractures of latex coatings taken in secondary electron (left) and backscattered electron mode (right): blank sample (a), sample  $L_{MgO-1.5\%}$  containing MgO-based nanoparticles (b), sample  $L_{ZnO-1.5\%}$  containing ZnO-based nanoparticles (c), sample  $L_{MgO+ZnO-1.75\%}$  containing MgO-based and ZnO-based nanoparticles (d), and sample  $L_{La_2O_3-1.5\%}$  containing  $La_2O_3$ -based nanoparticles (e).

### 3.3. Coating Properties

Although MeO nanoparticles were primarily used as antimicrobial additives, their effect on the structural properties of the coating film was also investigated. Nanoparticles of sparingly soluble MeOs have the potential to act as crosslinking agents providing ionic interfacial crosslinking, which significantly affects the properties of the resulting coating film [56]. For this reason, the level of crosslinking was examined from the point of view of the gel content, the average molecular weight between the crosslinking junctions ( $M_c$ ), and the crosslink density. As can be seen from the results (see Table 6), all types of MeO nanoparticles proved to be effective crosslinking agents. Compared to the blank coating (interfacially crosslinked by covalent bonds due to keto-hydrazide reaction), the crosslink density and gel content increased with MeO nanoparticle concentration, as has been evidenced by relevant literature dealing with nanostructured ZnO and MgO in self-crosslinking acrylic latex coatings. When comparing the individual MeO nanoparticles used, it was found that nanoparticulate MgO was the most effective crosslinking agent. This is probably due to its higher solubility, i.e., a higher concentration of dissociated divalent cations and thus an increased amount of neutralized carboxylic acid groups, as discussed above. We further believe that both surface carboxyl groups and those buried inside a latex particle were involved in ionic crosslinking, which provided inter- and intra-particle ionic crosslinks. In this perspective, it can be assumed that substantial intra-particle crosslinking already occurred during the synthesis of the polymer after the delivery of MgO nanoparticles. Furthermore, the measurements showed that  $\text{La}_2\text{O}_3$  provided coatings of a higher crosslink density than ZnO, which is in good accordance with theoretical solubility values (4.0 and 1.6 mg/L for  $\text{La}_2\text{O}_3$  and ZnO, respectively). A trivalent nature of the La cation may also play a role, binding more carboxyl groups than the divalent Zn cation. In the case of latexes combining MgO and ZnO nanoparticles, the degree of crosslinking corresponds to the contribution of the individual MeOs.

**Table 6.** Effect of the type and concentration of MeO nanoparticles on the degree of crosslinking.

Sample	Gel Content (%)	$M_c$ (g/mol)	Crosslink Density ( $\text{mol}/\text{cm}^3$ )
$L_0$	$72.7 \pm 0.3$	$76,500 \pm 600$	$1.49 \times 10^{-5}$
$L_{\text{MgO-0.5\%}}$	$89.4 \pm 0.2$	$19,500 \pm 300$	$5.74 \times 10^{-5}$
$L_{\text{MgO-1\%}}$	$92.1 \pm 0.3$	$14,700 \pm 300$	$7.53 \times 10^{-5}$
$L_{\text{MgO-1.5\%}}$	$95.9 \pm 0.4$	$7900 \pm 300$	$1.40 \times 10^{-4}$
$L_{\text{ZnO-0.5\%}}$	$86.0 \pm 0.1$	$29,500 \pm 500$	$3.84 \times 10^{-5}$
$L_{\text{ZnO-1\%}}$	$89.9 \pm 0.7$	$22,500 \pm 600$	$5.06 \times 10^{-5}$
$L_{\text{ZnO-1.5\%}}$	$91.0 \pm 0.5$	$16,500 \pm 100$	$6.73 \times 10^{-5}$
$L_{\text{MgO+ZnO-1.25\%}}$	$92.2 \pm 0.5$	$13,300 \pm 400$	$8.36 \times 10^{-5}$
$L_{\text{MgO+ZnO-1.5\%}}$	$95.4 \pm 0.4$	$8600 \pm 200$	$1.28 \times 10^{-4}$
$L_{\text{MgO+ZnO-1.75\%}}$	$96.5 \pm 0.6$	$7900 \pm 400$	$1.40 \times 10^{-4}$
$L_{\text{La}_2\text{O}_3-0.5\%}$	$91.2 \pm 0.3$	$26,200 \pm 500$	$4.43 \times 10^{-5}$
$L_{\text{La}_2\text{O}_3-1\%}$	$92.9 \pm 0.5$	$20,500 \pm 300$	$5.44 \times 10^{-5}$
$L_{\text{La}_2\text{O}_3-1.5\%}$	$95.3 \pm 0.6$	$12,900 \pm 300$	$8.67 \times 10^{-5}$

All testing of coating films cast on a substrate (glass or steel) was performed on coatings with a dry thickness of  $60 \pm 10 \mu\text{m}$ . The results of optical properties and water whitening are shown in Table 7. All prepared coating films were highly transparent and showed high gloss without the presence of defects, regardless of the type or concentration of embedded MeO nanoparticles. Due to the high transparency and gloss of the coating films, it can be assumed that the inorganic nanoparticles in the coating films occurred predominantly at the nanoscale, and during film formation, they did not impair the coalescence of the latex particles [110].

**Table 7.** Comparison of optical properties of coating films before after water exposure.

Sample	Before Water Exposure		Water Whitening Due to Water Exposure	
	Gloss (GU)	Transmittance (%) <sup>1</sup>	Transmittance (%) <sup>1</sup>	Decrease in Transmittance (rel.%)
L <sub>0</sub>	79.9 ± 0.5	89.5 ± 0.4	48.8 ± 0.3	45.5 ± 0.4
L <sub>MgO-0.5%</sub>	78.7 ± 0.8	90.1 ± 0.2	53.9 ± 0.4	40.2 ± 0.3
L <sub>MgO-1%</sub>	78.4 ± 0.3	90.3 ± 0.4	80.9 ± 0.3	10.4 ± 0.4
L <sub>MgO-1.5%</sub>	78.2 ± 0.5	89.7 ± 0.3	85.3 ± 0.5	4.9 ± 0.3
L <sub>ZnO-0.5%</sub>	80.0 ± 0.6	90.9 ± 0.5	49.5 ± 0.3	45.5 ± 0.4
L <sub>ZnO-1%</sub>	78.6 ± 0.4	90.0 ± 0.2	58.3 ± 0.4	35.2 ± 0.3
L <sub>ZnO-1.5%</sub>	78.6 ± 0.3	89.4 ± 0.3	68.7 ± 0.3	23.0 ± 0.3
L <sub>MgO+ZnO-1.25%</sub>	79.7 ± 0.5	89.9 ± 0.4	85.9 ± 0.3	5.3 ± 0.3
L <sub>MgO+ZnO-1.5%</sub>	79.9 ± 0.4	89.8 ± 0.3	86.7 ± 0.4	3.5 ± 0.4
L <sub>MgO+ZnO-1.75%</sub>	79.9 ± 0.2	89.9 ± 0.4	87.2 ± 0.5	3.0 ± 0.4
L <sub>La2O3-0.5%</sub>	78.0 ± 0.2	90.1 ± 0.2	54.5 ± 0.4	39.5 ± 0.3
L <sub>La2O3-1%</sub>	77.3 ± 0.3	90.6 ± 0.4	78.8 ± 0.3	13.0 ± 0.4
L <sub>La2O3-1.5%</sub>	77.6 ± 0.2	89.6 ± 0.3	87.6 ± 0.4	2.2 ± 0.3

<sup>1</sup> Value was measured at 500 nm.

As acrylic latex coatings show wretched water resistance (causing mainly swelling, whitening, and loss of adhesion to a substrate), water whitening testing was also performed. It is known that water whitening resistance increases with increasing crosslink density [29,111], because water whitening is caused by water domains in the coating film that exceed a certain size (light of longer wavelengths scatters more strongly with increasing domain size). Thus, if the polymer is strongly crosslinked, it contains only small water domains that appear less turbid to the human eye [29]. The measurement results showed in the case of all series of latex films that the level of water whitening decreased with increased MeO nanoparticle concentration and the results of water whitening were in good accordance with the crosslink density results shown in Table 6. It was found that latexes containing MgO (including the combination of MgO and ZnO) and La<sub>2</sub>O<sub>3</sub> nanoparticles at concentrations above 1 wt.% provided highly water whitening-resistant coating films. Based on the results, the crosslink density was shown to have the greatest influence on the water whitening resistance of coatings, which confirmed findings presented in previously published papers [55,56] on acrylic latexes containing nanostructured ZnO and MgO as functional additives.

The results of physical–mechanical properties, chemical resistance, and resistance to flash corrosion of coating films are shown in Table 8. Measurements of the surface hardness showed that coating hardness is affected by the increasing concentration of incorporated MeO nanoparticles. Coatings with embedded ZnO nanoparticles exhibited a lower surface hardness at lower nanoparticle concentrations in comparison with the reference (blank) coating. This phenomenon can be attributed to two competing effects, which are hydroplasticization (reducing hardness) and ionic interfacial crosslinking (increasing hardness), both phenomena being induced by dissolved Zn(OH)<sub>2</sub> molecules. For the latexes containing MgO nanoparticles, a pronounced decrease in coating hardness was found. This was probably due to the significant hydroplasticization of the carboxy-functionalized emulsion copolymer induced by the high extent of dissolved Mg(OH)<sub>2</sub> in the aqueous dispersion medium, as discussed above. In contrast, in latex coating films containing La<sub>2</sub>O<sub>3</sub> nanoparticles, a significant increase in surface hardness was found, which is probably due to a superior effect of ionic interfacial crosslinking (and increased rigidity of polymer chains) over hydroplasticization. The above-discussed competitive phenomena of hydroplasticization and ionic crosslinking can be very well observed in the case of latex coatings combining MgO and ZnO nanoparticles, where a reduced surface hardness was observed due to the presence of added MgO, which increased with increasing concentration of ZnO

nanoparticles, i.e., the effect of hydroplasticization of latex particles was slightly suppressed by the growing influence of ionic crosslinking.

**Table 8.** Comparison of physical—mechanical properties, chemical resistance, and resistance to flash corrosion of coating films.

Sample	Surface Hardness (rel.%)	Mechanical Properties		MEK Resistance (Strikes)	Flash Corrosion <sup>3</sup>	
		Impact Resistance (cm)	Adhesion (deg.)		ASTM D 610-85 (%)	Iodometric Scale (deg.)
L <sub>0</sub>	29.7 ± 0.9	10 ± 5	0 <sup>1</sup>	35 ± 7	>50 <sup>2</sup>	14
L <sub>MgO-0.5%</sub>	17.5 ± 1.0	>100 <sup>1</sup>	0	223 ± 16	>50	10
L <sub>MgO-1%</sub>	16.0 ± 1.2	>100	0	>300 <sup>1</sup>	10	1
L <sub>MgO-1.5%</sub>	13.2 ± 0.8	>100	0	>300	3	1
L <sub>ZnO-0.5%</sub>	24.6 ± 0.5	80 ± 5	0	196 ± 14	>50	11
L <sub>ZnO-1%</sub>	26.6 ± 0.7	45 ± 5	0	>300	16	1
L <sub>ZnO-1.5%</sub>	31.3 ± 1.1	35 ± 5	0	>300	16	1
L <sub>MgO+ZnO-1.25%</sub>	15.3 ± 0.5	>100	0	>300	16	1
L <sub>MgO+ZnO-1.5%</sub>	17.4 ± 0.9	>100	0	>300	10	1
L <sub>MgO+ZnO-1.75%</sub>	19.8 ± 0.7	>100	0	>300	10	1
L <sub>La2O3-0.5%</sub>	37.5 ± 0.8	20 ± 5	0	58 ± 5	>50	10
L <sub>La2O3-1%</sub>	40.0 ± 0.9	15 ± 5	0	178 ± 19	30	9
L <sub>La2O3-1.5%</sub>	41.5 ± 1.4	15 ± 5	0	213 ± 20	30	8

<sup>1</sup> Maximum evaluative value (representing the best property). <sup>2</sup> Minimum evaluative value (representing the worst property). <sup>3</sup> The results are given after performing an accelerated laboratory flash corrosion test.

Testing of mechanical properties showed that all coating samples showed increased impact resistance in contrast to the reference L<sub>0</sub>, which can be attributed mainly to hydroplasticization resulting in softening of the emulsion copolymer. Thus, latex coatings with MgO nanoparticles exceeded the maximum evaluation value compared to latex coatings containing only ZnO and La<sub>2</sub>O<sub>3</sub> nanoparticles, which is consistent with surface hardness and MFFT results. Adhesion testing showed that all samples exhibited the maximum possible evaluation value and therefore it can be stated that the type and concentration of the inserted nanoparticles did not reduce the adhesion of the coating film to the glass substrate.

The chemical resistance of the coating films was evaluated using the MEK test. The incorporation of nanoparticles was found to provide excellent MEK resistance of the coating films. This phenomenon was probably caused by the increased network density due to the formation of ionic bonds between the metal cations and the carboxyl groups of the polymer chains, as discussed above. Although latex films containing La<sub>2</sub>O<sub>3</sub> nanoparticles showed a high crosslink density, their resistance to MEK was found to be lower than for coating films containing ZnO nanoparticles (having a slightly lower crosslink density compared to La<sub>2</sub>O<sub>3</sub> latex coatings). This phenomenon can be explained by the trivalent nature of lanthanum in comparison with the divalent nature of magnesium and zinc ions, the former being able to bind more carboxyl groups. In this way, the La<sub>2</sub>O<sub>3</sub>-based network is mediated by fewer ionic crosslink junctions that are believed to be disrupted preferentially during the MEK test.

The disadvantage of water-based lacquers and paints is also the formation of the so-called flash corrosion after their application to a metal substrate, especially steel. Flash corrosion was evaluated according to the iodine scale, i.e., the coloration of the steel substrate by washing with Fe<sup>2+</sup> ions, and according to the ASTM D 610-85 standard, which was used to monitor corrosion centers. Flash corrosion was monitored after applying a latex coating to a steel substrate, and further after subjecting the coating to an accelerated laboratory test (see Table 8 and Figure 6). Before the accelerated test it was found that all types of nanoparticles provided increased resistance to flash corrosion with increasing concentration of embedded nanoparticles. Excellent results were provided in the systems

containing MgO nanoparticles, where no corrosion centers or steel substrate staining were monitored at all concentrations of embedded MgO nanoparticles, also in the case of the combinations of MgO and ZnO nanoparticles. In contrast, the results of the accelerated laboratory test revealed that latexes containing ZnO and La<sub>2</sub>O<sub>3</sub>-based nanoparticles did not show any significant effect on the inhibition of flash corrosion, while the latexes containing MgO-based nanoparticles provided a decrease in the number of microscopic corrosion centers with increasing MgO nanoparticle content. We are of the opinion that the pH value of the coating after the evaporation of ammonia (see pH data in Table 2) influences the formation of flash corrosion. The effect of alkaline pH on flash corrosion was described in the literature [60,63] and can be predicted using Pourbaix diagrams. The results for latex coatings with nanostructured ZnO and MgO, respectively, are in good agreement with our earlier papers [55,112].

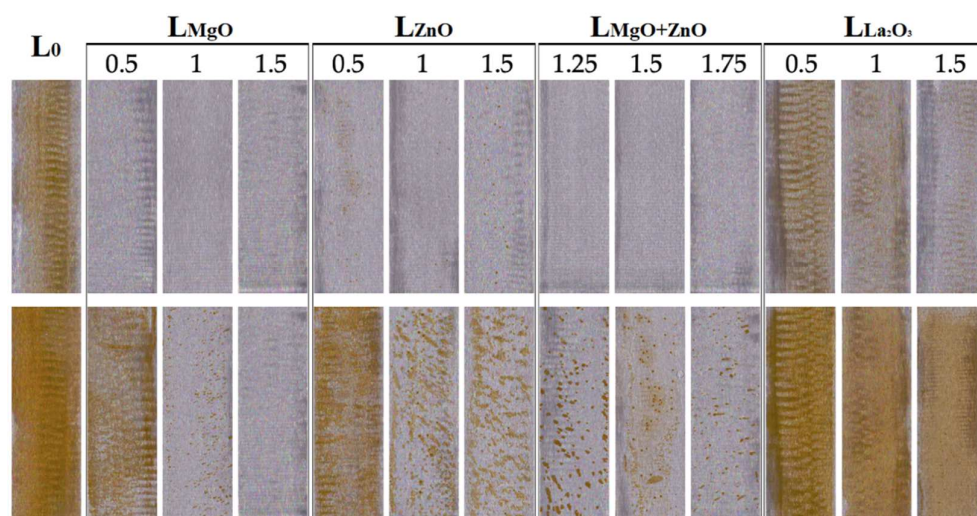


**Figure 6.** Flash corrosion testing before (**top**) and after (**bottom**) the accelerated laboratory flash corrosion test.

### 3.4. Antimicrobial Properties of Coating Films

The preparation of coatings with antimicrobial properties is an especially significant task today when the nosocomial infections occur more often due to antibiotic-resistant microbes. Moreover, a number of industrial products or buildings are facing the formation of biofilms. Here, we use the representants of both the gram-positive and gram-negative bacteria species. In our case, both gram-positive bacteria (*S. aureus*, *E. faecalis*) and gram-negative bacteria (*E. coli*, *K. pneumoniae*) were used to test the antibacterial activity of embedded inorganic nanoparticles in latex coating films. The bacterial strains of *S. aureus* and *E. coli* used are standard and the most tested bacteria to determine the antimicrobial efficacy of various materials. In contrast, the bacterial strain *K. pneumoniae* has been used due to the increased resistance of this hospital pathogen to a wide range of antibiotics [113,114], and the bacterial strain *E. faecalis* was chosen because of its high resistance to oxidative stress (by autoxidation it produces considerable extracellular superoxide and derivatives of reactive oxygen species) [115,116].

The antimicrobial efficacy of all prepared coating films according to modified ISO 22196 showed that the antibacterial efficacy increased with increasing concentration of embedded inorganic nanoparticles (see Table 9), which was also statistically confirmed using ANOVA (see Table S4). Photographic records are shown in Figures S7–S11. Furthermore, the tests revealed that for each MeO nanoparticle type at the highest concentration in a coating film (theoretically 1.5 wt.%, practically about 1.3 wt.%), the biocidal activity of coatings was achieved, except for the bacterium *E. faecalis*, against which only the coating containing the highest concentration of MgO nanoparticles showed biocidal activity, which confirmed findings presented in previously published papers [55,112] on acrylic

latexes containing nanostructured ZnO and MgO as functional additives. The undisputed resistance of *E. faecalis* to ZnO and La<sub>2</sub>O<sub>3</sub> nanoparticles can be explained by its higher resistance to oxidative stress, as mentioned above. In contrast, the biocidal efficiency of latex films with MgO nanoparticles can be explained by the high alkalinity of the coating film (see pH data in Table 2), which creates an unfavourable environment for MOs and, in addition, increases the activity of reactive oxygen species [83]. It should be emphasized here that the exact antimicrobial mechanism of MeO nanoparticles has not yet been clearly elucidated, but lipid peroxidation, the formation of reactive oxygen species, the presence of metal cations destroying MO enzymes, or the internalization of nanoparticles have been assumed [117–120]. It is further hypothesized that when metal cations enter a bacterial cell, the DNA molecule changes to a condensed form and loses its ability to replicate, leading to cell death [121,122]. The alkalinity of latexes may also play a role, whereas surface roughness (see Table S3), which is reported to affect the adhesion of MOs [123,124], was not found to significantly influence the antimicrobial efficacy of coatings.

**Table 9.** Results of antibacterial activity of coating films obtained using modified ISO 22196.

Sample	Growth of Bacterial Colonies <sup>1</sup>							
	<i>S. aureus</i>	Ø	<i>E. coli</i>	Ø	<i>E. faecalis</i>	Ø	<i>K. pneumoniae</i>	Ø
L <sub>0</sub>	5, 5, 5	5	5, 5, 5	5	5, 5, 5	5	5, 5, 5	5
L <sub>MgO-0.5%</sub>	5, 3, 3	4	4, 5, 5	5	3, 4, 4	4	1, 4, 1	2
L <sub>MgO-1%</sub>	1, 1, 3	2	5, 5, 5	5	2, 3, 3	3	0, 0, 0	0
L <sub>MgO-1.5%</sub>	0, 0, 0	0	0, 0, 0	0	0, 0, 0	0	0, 0, 0	0
L <sub>ZnO-0.5%</sub>	0, 2, 2	1	0, 0, 0	0	3, 3, 3	3	0, 0, 0	0
L <sub>ZnO-1%</sub>	0, 0, 1	0	0, 0, 0	0	3, 3, 3	3	0, 0, 0	0
L <sub>ZnO-1.5%</sub>	0, 0, 0	0	0, 0, 0	0	3, 3, 3	3	0, 0, 0	0
L <sub>MgO+ZnO-1.25%</sub>	4, 5, 4	4	5, 5, 5	5	4, 4, 4	4	5, 5, 4	5
L <sub>MgO+ZnO-1.5%</sub>	4, 3, 3	3	5, 5, 5	5	2, 3, 2	2	3, 3, 2	3
L <sub>MgO+ZnO-1.75%</sub>	0, 0, 0	0	1, 0, 0	0	1, 2, 1	1	0, 0, 0	0
L <sub>La2O3-0.5%</sub>	4, 5, 4	4	3, 4, 4	4	4, 4, 4	4	5, 5, 5	5
L <sub>La2O3-1%</sub>	1, 4, 4	3	0, 2, 2	1	4, 3, 3	3	5, 5, 3	4
L <sub>La2O3-1.5%</sub>	0, 0, 0	0	0, 0, 0	0	1, 2, 2	2	0, 0, 0	0

<sup>1</sup> The scale for assessing the growth of bacterial colonies: 0—without the growth; 1—the deductible amount on the 1st impression (individual colonies); 2—the deductible amount on the 1st impression (connected colonies); 3—the 2nd imprint of the recognizable colony, the 3rd imprint can be detected; 4—the 3rd imprint of the recognizable colony; 5—overgrown, continuous growth.

Based on the results obtained from the modified ISO 22196 standard, the most efficient sample in each prepared series of latexes was selected, namely L<sub>MgO-1.5%</sub>, L<sub>ZnO-1.5%</sub>, L<sub>MgO+ZnO-1.75%</sub>, L<sub>La2O3-1.5%</sub>, and tested for antibacterial activity according to ISO 22196. The results (see Table 10) were found to correlate with those obtained from the modified ISO 22196 standard (see Table 9), i.e., all latex coatings with inorganic nanoparticles showed biocidal activity against bacterial strains *S. aureus*, *E. coli*, and *K. pneumoniae* and latex coatings containing MgO nanoparticles provided biocidal activity also against the bacterial strain *E. faecalis* for the reasons discussed earlier. Photographic records are shown in Figure S12.

Analogous to the previous case, the testing of antifungal properties was performed only for the most efficient sample in each prepared series of latexes, namely L<sub>MgO-1.5%</sub>, L<sub>ZnO-1.5%</sub>, L<sub>MgO+ZnO-1.75%</sub>, L<sub>La2O3-1.5%</sub>, and the reference L<sub>0</sub>. The antifungal activity of embedded inorganic nanoparticles in latex coating films was evaluated against fungi *P. chrysogenum* and *A. brasiliensis* which are commonly found in temperate and subtropical regions, both in outdoor and indoor environments [125,126]. Testing was performed using a modified ASTM D5590 standard, which showed fungicidal efficacy only for coatings containing ZnO nanoparticles (L<sub>ZnO-1.5%</sub> and L<sub>MgO+ZnO-1.75%</sub>), see Table 11. The coating with La<sub>2</sub>O<sub>3</sub> nanoparticles provided a significant reduction in fungal growth, while the

coating with MgO nanoparticles exhibited moderate growth. Photographic records are shown in Figure S13. The high effectiveness of ZnO nanoparticles against fungi has already been discussed in the literature [127–129]. By analogy with the antibacterial mechanism, the mechanism for preventing the growth of fungi can be attributed to the formation of reactive oxygen species, electrostatic interaction leading to cell membrane damage, the release of metal ions, and internalization of nanoparticles, which also corresponds to the generally higher efficiency of ZnO nanoparticles at lower concentrations in antibacterial testing. The relative importance of these mechanisms depends on both the environment and the physical–mechanical properties of specific MeO nanoparticles.

**Table 10.** Results of antibacterial activity of coating films according to ISO 22196.

Sample	Antibacterial Properties <sup>1</sup>							
	<i>S. aureus</i>		<i>E. coli</i>		<i>E. faecalis</i>		<i>K. pneumoniae</i>	
	U <sub>t</sub>	R	U <sub>t</sub>	R	U <sub>t</sub>	R	U <sub>t</sub>	R
L <sub>0</sub>	5.6	-	6.5	-	4.9	-	4.1	-
L <sub>MgO-1.5%</sub>	0	>5.6	0	>6.5	0	>4.9	0	>4.1
L <sub>ZnO-1.5%</sub>	0	>5.6	0	>6.5	4.9	0	0	>4.1
L <sub>MgO+ZnO-1.75%</sub>	0	>5.6	0	>6.5	2.7	2.2	0	>4.1
L <sub>La2O3-1.5%</sub>	0	>5.6	0	>6.5	4.3	0.6	0	>4.1

<sup>1</sup> From the obtained values, the arithmetic mean was calculated, and recalculation was performed according to Equations (5) and (6) described in the theoretical part. R is antimicrobial activity and U<sub>t</sub> is the average value of the logarithm of viable bacteria in units of cells/cm<sup>2</sup> of untreated test samples after 24 h of incubation.

**Table 11.** Results of antifungal activity of coating films according to modified ASTM D5590.

Sample	Antifungal Properties <sup>1</sup>			
	<i>P. chrysogenum</i>	Ø	<i>A. brasiliensis</i>	Ø
L <sub>0</sub>	4, 4, 4	4	4, 4, 4	4
L <sub>MgO-1.5%</sub>	2, 3, 3	3	3, 2, 3	3
L <sub>ZnO-1.5%</sub>	0, 0, 0	0	0, 0, 0	0
L <sub>MgO+ZnO-1.75%</sub>	0, 0, 1	0	0, 0, 0	0
L <sub>La2O3-1.5%</sub>	0, 1, 1	1	1, 0, 1	1

<sup>1</sup> The scale for assessing the growth of fungi: 0—without the growth; 1—the trace of growth (<10%); 2—the growth (10%–30%); 3—the moderate growth (30%–70%); 4—the heavy growth (>70%).

#### 4. Conclusions

This work was devoted to the development of hygienic acrylic latexes which are expected to provide antimicrobial activity both in the liquid state and subsequently as a coating film on various substrates without the use of commercial (often toxic) biocidal additives. Various types of surface untreated MeO nanoparticles have been used as functional antimicrobial additives, namely MgO, ZnO, La<sub>2</sub>O<sub>3</sub>, and combinations of MgO and ZnO. To overcome the typical shortcomings of acrylic latexes, keto-hydrazide interfacial crosslinking has been introduced into the latexes. The inorganic nanoparticles were inserted into the latex during semi-continuous emulsion polymerization and latexes prepared in this way showed long-term stability. It was found that all used MeO nanoparticles provided antimicrobial properties and at the highest concentration used (theoretically 1.5 wt.%, practically about 1.3 wt.% in a dry coating film, and about 0.5 wt.% in liquid latex) ensured in-can antimicrobial stability of liquid latexes and bactericidal activity of coatings against three of four tested bacteria (*S. aureus*, *E. coli*, and *K. pneumoniae*). Only the coatings with the highest concentration of inserted MgO nanoparticles (1.31 wt.%) provided bactericidal activity against *E. faecalis*, probably due to the high alkalinity of the coatings caused by the hydration of MgO. In contrast, only latex coatings containing ZnO nanoparticles showed fungicidal activity, which is probably related to the highest concentration of reactive oxygen species formed in the case of ZnO nanoparticles. In addition to antimicrobial activity, the incorporation of MeO nanoparticles into acrylic latex was shown to provide

additional advantages. All types of inorganic nanoparticles were found to act as effective ionic crosslinkers, providing excellent resistance to MEK and water whitening without compromising the gloss and transparency of coatings. Furthermore, it was found that the incorporation of MgO nanoparticles into latex caused a significant decrease in MFFT due to hydroplasticization of the carboxy-functionalized emulsion copolymer, which was more pronounced with increasing concentration of MgO nanoparticles (converted predominantly to  $\text{Mg}(\text{OH})_2$ ). The insertion of MgO nanoparticles in latex also increased resistance to flash corrosion of steel substrates, including the number of microscopic corrosion centers, where at the highest concentration of nanoparticles, no corrosion center formation was evident, probably due to latex alkalinity. It can be concluded that environmentally-friendly one-component self-crosslinking latexes using MeO nanoparticles as antimicrobial additives and self-crosslinking agents were developed. These materials could be perfect binders for interior hygienic paints or clear coats providing durable protection for various materials including steel. Moreover, these latexes could also find application in exterior coatings which are particularly threatened by water and moisture, including microbial colonization.

**Supplementary Materials:** The following supporting information can be downloaded at: <https://www.mdpi.com/article/10.3390/coatings12101445/s1>, Table S1: Classification scale for the evaluation of coating damage according to CSN ISO 2409; Table S2: Gardner's iodometric scale.; Table S3: Surface roughness determined as RMS (root mean square parameter) of coating films according to ISO 4287; Table S4: Statistical ANOVA determination of the effect of concentration and type of nanoparticles on the antimicrobial activity of coatings; Figure S1: Sorting imprinted on three different agar areas for modified ISO 22196; Figure S2: Comparison of zeta potential distribution curves for latexes with the highest concentration of nanoparticles; Figure S3: XRD patterns of MgO inorganic nanoparticles: (A) originally supplied; (B) affected by polymerization conditions; Figure S4: XRD patterns of ZnO inorganic nanoparticles: (A) originally supplied; (B) affected by polymerization conditions; Figure S5: XRD patterns of  $\text{La}_2\text{O}_3$  inorganic nanoparticles: (A) originally supplied; (B) affected by polymerization conditions; Figure S6: The 3D visualisation of the topographical AFM scans: for blank sample  $L_0$  (a); sample  $L_{\text{MgO}-1.5\%}$  containing MgO-based nanoparticles (b); sample  $L_{\text{ZnO}-1.5\%}$  containing ZnO-based nanoparticles (c), sample  $L_{\text{MgO}+\text{ZnO}-1.75\%}$  containing MgO-based and ZnO-based nanoparticles (d) and sample  $L_{\text{La}_2\text{O}_3-1.5\%}$  containing  $\text{La}_2\text{O}_3$ -based nanoparticles (e); Figure S7: Antimicrobial efficiency of  $L_0$  latex-based coating film according to modified ISO 22196; Figure S8: Antimicrobial efficiency of  $L_{\text{MgO}}$  latex-based coating films according to modified ISO 22196; Figure S9: Antimicrobial efficiency of  $L_{\text{ZnO}}$  latex-based coating films according to modified ISO 22196; Figure S10: Antimicrobial efficiency of  $L_{\text{MgO}+\text{ZnO}}$  latex-based coating films according to modified ISO 22196; Figure S11: Antimicrobial efficiency of  $L_{\text{La}_2\text{O}_3}$  latex-based coating films according to modified ISO 22196; Figure S12: Antimicrobial efficiency of coating films according to ISO 22196; Figure S13: Antifungal efficacy of coating films on wood panels against *A. brasiliensis*.

**Author Contributions:** Conceptualization, D.S., A.K. (Andréa Kalendová) and J.M.; methodology, J.M. and P.H.; software, D.S.; validation, D.S. and J.M.; formal analysis, J.M.; investigation, D.S., P.K., J.V., S.S., A.K. (Anna Krejčová), L.B. and F.W.-F.; resources, D.S. and J.M.; data curation, A.K. (Anna Krejčová); writing—original draft preparation, D.S. and J.M.; writing—review and editing, D.S. and J.M.; visualization, D.S.; supervision, A.K. (Andréa Kalendová). All authors have read and agreed to the published version of the manuscript.

**Funding:** This research was funded by the Ministry of Education, Youth and Sports of the Czech Republic (project LM2018103). Authors PH and JV express thanks for project support from the Ministry of Education, Youth and Sports of the Czech Republic—DKRVO (RP/CPS/2022/001).

**Institutional Review Board Statement:** Not applicable.

**Informed Consent Statement:** Not applicable.

**Data Availability Statement:** Data sharing is not applicable to this article.

**Conflicts of Interest:** The authors declare no conflict of interest.

## References

1. Faccini, M.; Bautista, L.; Soldi, L.; Escobar, A.M.; Altavilla, M.; Calvet, M.; Domenech, A.; Domínguez, E. Environmentally friendly anticorrosive polymeric coatings. *Appl. Sci.* **2021**, *11*, 3446. [[CrossRef](#)]
2. Noreen, A.; Zia, K.M.; Zuber, M.; Tabasum, S.; Saif, M.J. Recent trends in environmentally friendly water-borne polyurethane coatings: A review. *Korean J. Chem. Eng.* **2016**, *33*, 388–400. [[CrossRef](#)]
3. Berenjian, A.; Chang, N.; Malmiri, H.J. Volatile organic compounds removal methods: A review. *Am. J. Biochem. Biotechnol.* **2012**, *8*, 220–229. [[CrossRef](#)]
4. Maniglia, B.C.; Castanha, N.; Le Bail, P.; Le Bail, A.; Augusto, P.E.D. Starch modification through environmentally friendly alternatives: A review. *Crit. Rev. Food Sci. Nutr.* **2021**, *61*, 2482–2505. [[CrossRef](#)]
5. Fulmer, P.A.; Wynne, J.H. Development of Broad-Spectrum Antimicrobial Latex Paint Surfaces Employing Active Amphiphilic Compounds. *ACS Appl. Mater. Interfaces* **2011**, *3*, 2878–2884. [[CrossRef](#)]
6. Bellotti, N.; Deyá, C. Waterborne functional paints to control biodeterioration. In *Handbook of Waterborne Coatings*; Elsevier: Amsterdam, The Netherlands, 2020; pp. 155–179. ISBN 9780128142011. [[CrossRef](#)]
7. Han, W.; Wu, Z.; Li, Y.; Wang, Y. Graphene family nanomaterials (GFNs)—Promising materials for antimicrobial coating and film: A review. *Chem. Eng. J.* **2019**, *358*, 1022–1037. [[CrossRef](#)]
8. Cloutier, M.; Mantovani, D.; Rosei, F. Antibacterial Coatings: Challenges, Perspectives, and Opportunities. *Trends Biotechnol.* **2015**, *33*, 637–652. [[CrossRef](#)]
9. Chen, L.; Song, X.; Xing, F.; Wang, Y.; Wang, Y.; He, Z.; Sun, L. A Review on Antimicrobial Coatings for Biomaterial Implants and Medical Devices. *J. Biomed. Nanotechnol.* **2020**, *16*, 789–809. [[CrossRef](#)]
10. Mishra, P.K.; Giagli, K.; Tsalagkas, D.; Mishra, H.; Talegaonkar, S.; Gryc, V.; Wimmer, R. Changing Face of Wood Science in Modern Era: Contribution of Nanotechnology. *Recent Pat. Nanotechnol.* **2018**, *12*, 13–21. [[CrossRef](#)]
11. Athawale, V.D.; Nimbalkar, R.V. Waterborne Coatings Based on Renewable Oil Resources: An Overview. *J. Am. Oil Chem. Soc.* **2011**, *88*, 159–185. [[CrossRef](#)]
12. Parvate, S.; Mahanwar, P. Advances in self-crosslinking of acrylic emulsion: What we know and what we would like to know. *J. Dispers. Sci. Technol.* **2019**, *40*, 519–536. [[CrossRef](#)]
13. Mariz, I.d.F.A.; Millichamp, I.S.; de la Cal, J.C.; Leiza, J.R. High performance water-borne paints with high volume solids based on bimodal latexes. *Prog. Org. Coat.* **2010**, *68*, 225–233. [[CrossRef](#)]
14. Khaletskaya, K.; Khaletski, V.; Švedienė, S.; Mažeikienė, A. Environmental-friendly architectural water-borne paint for outdoor application: Twenty years of experience in Belarus and Lithuania. In Proceedings of the 9th International Conference “ENVIRONMENTAL ENGINEERING”, Vilnius, Lithuania, 22–23 May 2014; pp. 1–5.
15. Sørensen, P.A.; Kiil, S.; Dam-Johansen, K.; Weinell, C.E. Anticorrosive coatings: A review. *J. Coat. Technol. Res.* **2009**, *6*, 135–176. [[CrossRef](#)]
16. Wagle, P.G.; Tamboli, S.S.; More, A.P. Peelable coatings: A review. *Prog. Org. Coat.* **2021**, *150*, 106005. [[CrossRef](#)]
17. Overbeek, A.; Bückmann, F.; Martin, E.; Steenwinkel, P.; Annable, T. New generation decorative paint technology. *Prog. Org. Coat.* **2003**, *48*, 125–139. [[CrossRef](#)]
18. Bauer, P.; Denk, P.; Fuss, J.M.; Lorber, K.; Ortner, E.; Buettner, A. Correlations between odour activity and the structural modifications of acrylates. *Anal. Bioanal. Chem.* **2019**, *411*, 5545–5554. [[CrossRef](#)]
19. McCready, D. A tiered approach for assessing dermal exposure to constituents in latex paint. *Hum. Ecol. Risk Assess.* **2009**, *15*, 1227–1244. [[CrossRef](#)]
20. Wu, S.; Soucek, M.D. Model compound study for acrylic latex crosslinking reactions with cycloaliphatic epoxides. *J. Coat. Technol.* **1997**, *69*, 43–49. [[CrossRef](#)]
21. Tillet, G.; Boutevin, B.; Ameduri, B. Chemical reactions of polymer crosslinking and post-crosslinking at room and medium temperature. *Prog. Polym. Sci.* **2011**, *36*, 191–217. [[CrossRef](#)]
22. González, I.; Asua, J.M.; Leiza, J.R. Crosslinking in Acetoacetoxy Functional Waterborne Crosslinkable Latexes. *Macromol. Symp.* **2006**, *243*, 53–62. [[CrossRef](#)]
23. Machotová, J.; Kalendová, A.; Steinerová, D.; Mácová, P.; Šlang, S.; Šňupárek, J.; Vajdák, J. Water-Resistant Latex Coatings: Tuning of Properties by Polymerizable Surfactant, Covalent Crosslinking and Nanostructured ZnO Additive. *Coatings* **2021**, *11*, 347. [[CrossRef](#)]
24. Taylor, J.W.; Winnik, M.A. Functional latex and thermoset latex films. *J. Coat. Technol. Res.* **2004**, *1*, 163–190. [[CrossRef](#)]
25. Ooka, M.; Ozawa, H. Recent developments in crosslinking technology for coating resins. *Prog. Org. Coat.* **1994**, *23*, 325–338. [[CrossRef](#)]
26. Machotová, J.; Knotek, P.; Černošková, E.; Svoboda, R.; Zárybnická, L.; Kohl, M.; Kalendová, A. Effect of Fluorinated Comonomer, Polymerizable Emulsifier, and Crosslinking on Water Resistance of Latex Coatings. *Coatings* **2022**, *12*, 1150. [[CrossRef](#)]
27. Fred, B.; Ad, O.T.N.; Tijis, N. Self Crosslinking Surfactant Free Acrylic Dispersion. *Eur. Coat. J.* **2001**, *6*, 53–60.
28. Nakayama, Y. Development of novel aqueous coatings which meet the requirements of ecology-conscious society: Novel cross-linking system based on the carbonyl-hydrazide reaction and its applications. *Prog. Org. Coat.* **2004**, *51*, 280–299. [[CrossRef](#)]
29. Kessel, N.; Illsley, D.R.; Keddie, J.L. The diacetone acrylamide crosslinking reaction and its influence on the film formation of an acrylic latex. *J. Coat. Technol. Res.* **2008**, *5*, 285–297. [[CrossRef](#)]

30. Koukiotis, C.; Sideridou, I.D. Synthesis and characterization of latexes based on copolymers BA\MMA\DAAM and BA\MMA\VEOVA-10\DAAM and the corresponding 1K crosslinkable binder using the adipic acid dihydrazide as crosslinking agent. *Prog. Org. Coat.* **2010**, *69*, 504–509. [[CrossRef](#)]
31. Machotová, J.; Černošková, E.; Honzíček, J.; Šňupárek, J. Water sensitivity of fluorine-containing polyacrylate latex coatings: Effects of crosslinking and ambient drying conditions. *Prog. Org. Coat.* **2018**, *120*, 266–273. [[CrossRef](#)]
32. Guo, T.-Y.; Liu, J.-C.; Song, M.-D.; Zhang, B.-H. Effects of carboxyl group on the ambient self-crosslinkable polyacrylate latices. *J. Appl. Polym. Sci.* **2007**, *104*, 3948–3953. [[CrossRef](#)]
33. Zhang, X.; Liu, Y.; Huang, H.; Li, Y.; Chen, H. The diacetone acrylamide crosslinking reaction and its control of core-shell polyacrylate latices at ambient temperature. *J. Appl. Polym. Sci.* **2012**, *123*, 1822–1832. [[CrossRef](#)]
34. Guiamet, P.S.; Videla, H.A. Microbiological Spoilage of Aqueous Based Surface Coatings. *Corros. Rev.* **1996**, *14*, 47–58. [[CrossRef](#)]
35. Samyn, P.; Bosmans, J.; Cossemans, P. Current Alternatives for In-Can Preservation of Aqueous Paints: A Review. *Mater. Proceeding* **2021**, *7*, 18. [[CrossRef](#)]
36. Silva, V.; Silva, C.; Soares, P.; Garrido, E.M.; Borges, F.; Garrido, J. Isothiazolinone Biocides: Chemistry, Biological, and Toxicity Profiles. *Molecules* **2020**, *25*, 991. [[CrossRef](#)]
37. Okamura, H.; Togosmaa, L.; Sawamoto, T.; Fukushi, K.; Nishida, T.; Beppu, T. Effects of metal pyrithione antifoulants on freshwater macrophyte *Lemna gibba* G3 determined by image analysis. *Ecotoxicology* **2012**, *21*, 1102–1111. [[CrossRef](#)]
38. Amara, I.; Miled, W.; Slama, R.B.; Ladhari, N. Antifouling processes and toxicity effects of antifouling paints on marine environment. A review. *Environ. Toxicol. Pharmacol.* **2018**, *57*, 115–130. [[CrossRef](#)]
39. Glinel, K.; Thebault, P.; Humblot, V.; Pradier, C.M.; Jouenne, T. Antibacterial surfaces developed from bio-inspired approaches. *Acta Biomater.* **2012**, *8*, 1670–1684. [[CrossRef](#)]
40. Kandelbauer, A.; Widsten, P. Antibacterial melamine resin surfaces for wood-based furniture and flooring. *Prog. Org. Coat.* **2009**, *65*, 305–313. [[CrossRef](#)]
41. Fonkwo, P.N. Pricing infectious disease. *EMBO Rep.* **2008**, *9*, 13–17. [[CrossRef](#)]
42. Sánchez-López, E.; Gomes, D.; Esteruelas, G.; Bonilla, L.; Lopez-Machado, A.L.; Galindo, R.; Cano, A.; Espina, M.; Ettcheto, M.; Camins, A.; et al. Metal-Based Nanoparticles as Antimicrobial Agents: An Overview. *Nanomaterials* **2020**, *10*, 292. [[CrossRef](#)]
43. Wang, L.; Hu, C.; Shao, L. The antimicrobial activity of nanoparticles: Present situation and prospects for the future. *Int. J. Nanomed.* **2017**, *12*, 1227–1249. [[CrossRef](#)] [[PubMed](#)]
44. Azam, A.; Ahmed, A.S.; Oves, M.; Khan, M.S.; Habib, S.S.; Memic, A. Antimicrobial activity of metal oxide nanoparticles against Gram-positive and Gram-negative bacteria: A comparative study. *Int. J. Nanomed.* **2012**, *7*, 6003–6009. [[CrossRef](#)]
45. Dizaj, S.M.; Lotfipour, F.; Barzegar-Jalali, M.; Zarrintan, M.H.; Adibkia, K. Antimicrobial activity of the metals and metal oxide nanoparticles. *Mater. Sci. Eng. C* **2014**, *44*, 278–284. [[CrossRef](#)]
46. Bonnefond, A.; González, E.; Asua, J.M.; Leiza, J.R.; Kiwi, J.; Pulgarin, C.; Rtimi, S. New evidence for hybrid acrylic/TiO<sub>2</sub> films inducing bacterial inactivation under low intensity simulated sunlight. *Colloids Surf. B Biointerfaces* **2015**, *135*, 1–7. [[CrossRef](#)]
47. Yilmaz Atay, H.; Yaşa, İ.; Çelik, E. Antibacterial Polymeric Coatings with Synthesized Silver Nanoparticles. *Synth. React. Inorg. Met.-Org. Nano-Met. Chem.* **2015**, *45*, 784–798. [[CrossRef](#)]
48. Thurman, R.B.; Gerba, C.P.; Bitton, G. The molecular mechanisms of copper and silver ion disinfection of bacteria and viruses. *Crit. Rev. Environ. Control* **1989**, *18*, 295–315. [[CrossRef](#)]
49. Domek, M.J.; Lechevallier, M.W.; Cameron, S.C.; Mcfeters, G.A. Evidence for the role of copper in the injury process of coliform bacteria in drinking water. *Appl. Environ. Microbiol.* **1984**, *48*, 289–293. [[CrossRef](#)] [[PubMed](#)]
50. Chandrangsu, P.; Rensing, C.; Helmann, J.D. Metal homeostasis and resistance in bacteria. *Nat. Rev. Microbiol.* **2017**, *15*, 338–350. [[CrossRef](#)]
51. Brabu, B.; Haribabu, S.; Revathy, M.; Anitha, S.; Thangapadian, M.; Navaneethakrisnan, K.R.; Gopalakrishnan, C.; Murugan, S.S.; Kumaavel, T.S. Biocompatibility studies on lanthanum oxide nanoparticles. *Toxicol. Res.* **2015**, *4*, 1037–1044. [[CrossRef](#)]
52. Schopf, J.W.; Kudryavtsev, A.B.; Agresti, D.G.; Wdowiak, T.J.; Czaja, D. Laser-Raman imagery of Earth's earliest fossils. *Nature* **2002**, *416*, 73–76. [[CrossRef](#)]
53. Mekhemer, G.A.H. Surface structure and acid–base properties of lanthanum oxide dispersed on silica and alumina catalysts. *Phys. Chem. Chem. Phys.* **2002**, *4*, 5400–5405. [[CrossRef](#)]
54. Yan, W.; Zhang, X.; Zhu, Y.; Chen, H. Synthesis and characterization of self-crosslinkable zinc polyacrylate latices at room temperature. *Iran. Polym. J.* **2012**, *21*, 631–639. [[CrossRef](#)]
55. Machotová, J.; Kalendová, A.; Voleská, M.; Steinerová, D.; Pejchalová, M.; Knotek, P.; Zárbybnická, L. Waterborne hygienic coatings based on self-crosslinking acrylic latex with embedded inorganic nanoparticles: A comparison of nanostructured ZnO and MgO as antibacterial additives. *Prog. Org. Coat.* **2020**, *147*, 105704. [[CrossRef](#)]
56. Machotová, J.; Kalendová, A.; Zlámaná, B.; Šňupárek, J.; Palarčík, J.; Svoboda, R. Waterborne coating binders based on self-crosslinking acrylic latex with embedded inorganic nanoparticles: A comparison of nanostructured ZnO and MgO as crosslink density enhancing agents. *Coatings* **2020**, *10*, 339. [[CrossRef](#)]
57. Zosel, A. Mechanical properties of films from polymer latices. *Polym. Adv. Technol.* **1995**, *6*, 263–269. [[CrossRef](#)]
58. Kan, C.S.; Blackson, J.H. Effect of Ionomeric Behavior on the Viscoelastic Properties and Morphology of Carboxylated Latex Films. *Macromolecules* **1996**, *29*, 6853–6864. [[CrossRef](#)]

59. Richard, J.; Maquet, J. Dynamic micromechanical investigations into particle/particle interfaces in latex films. *Polymer* **1992**, *33*, 4164–4173. [[CrossRef](#)]
60. Machotova, J.; Ruckerova, A.; Bohacik, P.; Pukova, K.; Kalendova, A.; Palarcik, J. High-performance one-pack ambient cross-linking latex binders containing low-generation PAMAM dendrimers and ZnO nanoparticles. *J. Coat. Technol. Res.* **2018**, *15*, 1167–1179. [[CrossRef](#)]
61. Lee, D.I. The effects of latex coalescence and interfacial crosslinking on the mechanical properties of latex films. *Polymer* **2005**, *46*, 1287–1293. [[CrossRef](#)]
62. Danková, M.; Kalendová, A.; Machotová, J. Waterborne coatings based on acrylic latex containing nanostructured ZnO as an active additive. *J. Coat. Technol. Res.* **2020**, *17*, 517–529. [[CrossRef](#)]
63. Kalendová, A. Methods for testing and evaluating the flash corrosion. *Prog. Org. Coat.* **2002**, *44*, 201–209. [[CrossRef](#)]
64. Novák, P. Druhy koroze kovů. *Koroze A Ochr. Mater.* **2005**, *49*, 75–82.
65. Verink, E.D. Simplified procedure for constructing Pourbaix diagrams. *Uhlig's Corros. Handb.* **2011**, *7*, 111–124. [[CrossRef](#)]
66. Steinerová, D.; Kalendová, A.; Machotová, J.; Pejchalová, M. Environmentally Friendly Water-Based Self-Crosslinking Acrylate Dispersion Containing Magnesium Nanoparticles and Their Films Exhibiting Antimicrobial Properties. *Coatings* **2020**, *10*, 340. [[CrossRef](#)]
67. Bharadwaj, H.K.; Lee, J.-Y.; Li, X.; Liu, Z.; Keener, T.C. Dissolution kinetics of magnesium hydroxide for CO<sub>2</sub> separation from coal-fired power plants. *J. Hazard. Mater.* **2013**, *250–251*, 292–297. [[CrossRef](#)]
68. Kong, B.; Seog, J.H.; Graham, L.M.; Lee, S.B. Experimental considerations on the cytotoxicity of nanoparticles. *Nanomedicine* **2011**, *6*, 929–941. [[CrossRef](#)]
69. Lewinski, N.; Colvin, V.; Drezek, R. Cytotoxicity of Nanoparticles. *Small* **2008**, *4*, 26–49. [[CrossRef](#)]
70. Pinho, A.R.; Martins, F.; Costa, M.E.V.; Senos, A.M.R.; da Cruz e Silva, O.A.B.; Pereira, M.d.L.; Rebelo, S. In Vitro Cytotoxicity Effects of Zinc Oxide Nanoparticles on Spermatogonia Cells. *Cells* **2020**, *9*, 1081. [[CrossRef](#)] [[PubMed](#)]
71. Pandurangan, M.; Kim, D.H. In vitro toxicity of zinc oxide nanoparticles: A review. *J. Nanoparticle Res.* **2015**, *17*, 158. [[CrossRef](#)]
72. Mahmoud, A.; Ezgi, Ö.; Merve, A.; Özhan, G. In Vitro Toxicological Assessment of Magnesium Oxide Nanoparticle Exposure in Several Mammalian Cell Types. *Int. J. Toxicol.* **2016**, *35*, 429–437. [[CrossRef](#)]
73. Patel, M.K.; Zafaryab, M.; Rizvi, M.M.A.; Agrawal, V.V.; Ansari, Z.A.; Malhotra, B.D.; Ansari, S.G. Antibacterial and Cytotoxic Effect of Magnesium Oxide Nanoparticles on Bacterial and Human Cells. *J. Nanoeng. Nanomanufacturing* **2013**, *3*, 162–166. [[CrossRef](#)]
74. Dong, Q.; Ge, S.; Shen, Y.; Wang, H.; Yin, T.; Wang, G.; Jia, D.; Zhang, Q. Cytotoxic effects of MgO nanoparticles on human umbilical vein endothelial cells in vitro. *IET Nanobiotechnol.* **2011**, *5*, 36–40. [[CrossRef](#)]
75. Balusamy, B.; Taştan, B.E.; Ergen, S.F.; Uyar, T.; Tekinay, T. Toxicity of lanthanum oxide (La<sub>2</sub>O<sub>3</sub>) nanoparticles in aquatic environments. *Environ. Sci. Process. Impacts* **2015**, *17*, 1265–1270. [[CrossRef](#)] [[PubMed](#)]
76. Almukhlafi, H.; Ali, D.; Almutairi, B.; Yaseen, K.N.; Alyami, N.; Almeer, R.; Alkahtani, S.; Alarifi, S. Role of Oxidative Stress in La<sub>2</sub>O<sub>3</sub> Nanoparticle-Induced Cytotoxicity and Apoptosis in CHANG and HuH-7 Cells. *Int. J. Nanomed.* **2021**, *16*, 3487–3496. [[CrossRef](#)] [[PubMed](#)]
77. Lu, V.M.; Jue, T.R.; McDonald, K.L. Cytotoxic lanthanum oxide nanoparticles sensitize glioblastoma cells to radiation therapy and temozolomide: An in vitro rationale for translational studies. *Sci. Rep.* **2020**, *10*, 18156. [[CrossRef](#)] [[PubMed](#)]
78. Zhu, X.; Zhu, L.; Duan, Z.; Qi, R.; Li, Y.; Lang, Y. Comparative toxicity of several metal oxide nanoparticle aqueous suspensions to Zebrafish (Danio rerio) early developmental stage. *J. Environ. Sci. Health Part A* **2008**, *43*, 278–284. [[CrossRef](#)]
79. Blinova, I.; Ivask, A.; Heinlaan, M.; Mortimer, M.; Kahru, A. Ecotoxicity of nanoparticles of CuO and ZnO in natural water. *Environ. Pollut.* **2010**, *158*, 41–47. [[CrossRef](#)]
80. Sharma, V.; Shukla, R.K.; Saxena, N.; Parmar, D.; Das, M.; Dhawan, A. DNA damaging potential of zinc oxide nanoparticles in human epidermal cells. *Toxicol. Lett.* **2009**, *185*, 211–218. [[CrossRef](#)]
81. Esmaeillou, M.; Moharamnejad, M.; Hsankhani, R.; Tehrani, A.A.; Maadi, H. Toxicity of ZnO nanoparticles in healthy adult mice. *Environ. Toxicol. Pharmacol.* **2013**, *35*, 67–71. [[CrossRef](#)]
82. Sharma, V.; Singh, P.; Pandey, A.K.; Dhawan, A. Induction of oxidative stress, DNA damage and apoptosis in mouse liver after sub-acute oral exposure to zinc oxide nanoparticles. *Mutat. Res. Genet. Toxicol. Environ. Mutagen.* **2012**, *745*, 84–91. [[CrossRef](#)]
83. Abbasalipourkabir, R.; Moradi, H.; Zarei, S.; Asadi, S.; Salehzadeh, A.; Ghafourikhosroshahi, A.; Mortazavi, M.; Ziamajidi, N. Toxicity of zinc oxide nanoparticles on adult male Wistar rats. *Food Chem. Toxicol.* **2015**, *84*, 154–160. [[CrossRef](#)] [[PubMed](#)]
84. Xiao, L.; Liu, C.; Chen, X.; Yang, Z. Zinc oxide nanoparticles induce renal toxicity through reactive oxygen species. *Food Chem. Toxicol.* **2016**, *90*, 76–83. [[CrossRef](#)] [[PubMed](#)]
85. Banyal, S.; Malik, P.; Tuli, H.S.; Mukherjee, T.K. Advances in nanotechnology for diagnosis and treatment of tuberculosis. *Curr. Opin. Pulm. Med.* **2013**, *19*, 289–297. [[CrossRef](#)]
86. Fox, T.G.; Flory, P.J. Second-Order Transition Temperatures and Related Properties of Polystyrene. I. Influence of Molecular Weight. *J. Appl. Phys.* **1950**, *21*, 581–591. [[CrossRef](#)]
87. Covington, A.K.; Bates, R.G.; Durst, R.A. Definition of pH scales, standard reference values, measurement of pH and related terminology. *Pure Appl. Chem.* **1985**, *57*, 531–542. [[CrossRef](#)]
88. Bhattacharjee, S. DLS and zeta potential—What they are and what they are not? *J. Control. Release* **2016**, *235*, 337–351. [[CrossRef](#)]

89. Diesel Fuel Test Kit. Available online: [https://www.dieselfueltestkit.com/ft-bug-test-kit-for-diesel-bacteria-testing/?fbclid=IwAR0ASDDOfCHmNW3i2lvPRehl0oK7ORC7M80fE\\_Hc3t2voVMGupCC91V2BHM](https://www.dieselfueltestkit.com/ft-bug-test-kit-for-diesel-bacteria-testing/?fbclid=IwAR0ASDDOfCHmNW3i2lvPRehl0oK7ORC7M80fE_Hc3t2voVMGupCC91V2BHM) (accessed on 27 March 2022).
90. Kalendová, A. *Technologie Nátěrových Hmot II: Povrchové Úpravy a Způsoby Předúpravy Materiálů*, 1st ed.; Univerzita Pardubice: Pardubice, Czech Republic, 2003; pp. 51–128. ISBN 80-7194-576-5.
91. Cline, J.P.; von Dreele, R.B.; Winburn, R.; Stephens, P.W.; Filliben, J.J. Addressing the amorphous content issue in quantitative phase analysis: The certification of NIST standard reference material 676a. *Acta Crystallogr. Sect. A Found. Crystallogr.* **2011**, *67*, 357–367. [[CrossRef](#)]
92. Moore, G.L. *Introduction to Inductively Coupled Plasma Atomic Emission Spectrometry*, 1st ed.; Elsevier Science: Randburg, South Africa, 1988; pp. 1–309. ISBN 9780444599070.
93. Flory, P.J.; Rehner, J. Statistical Mechanics of Cross-Linked Polymer Networks II. Swelling. *J. Chem. Phys.* **1943**, *11*, 521–526. [[CrossRef](#)]
94. Tobing, S.; Klein, A. Molecular Parameters and Their Relation to the Adhesive Performance of Emulsion Acrylic Pressure-Sensitive Adhesives. *J. Appl. Polym. Sci.* **2001**, *79*, 2230–2244. [[CrossRef](#)]
95. Vandenburg, H.J.; Clifford, A.A.; Bartle, K.D.; Carlson, R.E.; Carroll, J.; Newton, I.D. A simple solvent selection method for accelerated solvent extraction of additives from polymers. *Analyst* **1999**, *124*, 1707–1710. [[CrossRef](#)]
96. Habib, S.; Lehocky, M.; Vesela, D.; Humpolíček, P.; Krupa, I.; Popelka, A. Preparation of Progressive Antibacterial LDPE Surface via Active Biomolecule Deposition Approach. *Polymers* **2019**, *11*, 1704. [[CrossRef](#)]
97. Adan, O.C.G. *The Fungal Resistance of Interior Finishing Materials. Fundamentals of Mold Growth in Indoor Environments and Strategies for Healthy Living*, 1st ed.; Wageningen Academic Publishers: Wageningen, The Netherlands, 2011; pp. 335–352. ISBN 978-90-8686-722-6.
98. Machotová, J.; Kalendová, A.; Pejchalová, M.; Danková, M.; Palarčík, J. Samosíťující latexy s antibakteriálním účinkem a chemickou odolností nátěrových povlaků. *Chem. Listy* **2020**, *114*, 285–290.
99. Patnaik, P. *Handbook of Inorganic Chemicals*; McGraw-Hill: New York, NY, USA, 2003; p. 5299. ISBN 00-704-9439-8.
100. Tsavalas, J.G.; Sundberg, D.C. Hydroplasticization of Polymers: Model Predictions and Application to Emulsion Polymers. *Langmuir* **2010**, *26*, 6960–6966. [[CrossRef](#)] [[PubMed](#)]
101. Jiang, B.; Tsavalas, J.G.; Sundberg, D.C. Water whitening of polymer films: Mechanistic studies and comparisons between water and solvent borne films. *Prog. Org. Coat.* **2017**, *105*, 56–66. [[CrossRef](#)]
102. Horský, J.; Quadrat, O.; Porsch, B.; Mrkvičková, L.; Šňupárek, J. Effect of alkalization on carboxylated latices prepared with various amount of a non-ionogenic hydrophilic comonomer 2-hydroxyethyl methacrylate. *Colloids Surf. A Physicochem. Eng. Asp.* **2001**, *180*, 75–85. [[CrossRef](#)]
103. Bernal, S.; Botana, F.J.; García, R.; Rodríguez-Izquierdo, J.M. Behaviour of rare earth sesquioxides exposed to atmospheric carbon dioxide and water. *React. Solids* **1987**, *4*, 23–40. [[CrossRef](#)]
104. Matsuzawa, K.; Mizusaki, T.; Mitsushima, S.; Kamiya, N.; Ota, K. The effect of La oxide additive on the solubility of NiO in molten carbonates. *J. Power Sources* **2005**, *140*, 258–263. [[CrossRef](#)]
105. Bernal, S.; Botana, F.J.; García, R.; Rodríguez-Izquierdo, J.M. Thermal evolution of a sample of La<sub>2</sub>O<sub>3</sub> exposed to the atmosphere. *Thermochim. Acta* **1983**, *66*, 139–145. [[CrossRef](#)]
106. Balducci, G.; Diaz, L.B.; Gregory, D.H. Recent progress in the synthesis of nanostructured magnesium hydroxide. *CrystEngComm* **2017**, *19*, 6067–6084. [[CrossRef](#)]
107. Knotek, P.; Chanova, E.; Rypacek, F. AFM imaging and analysis of local mechanical properties for detection of surface pattern of functional groups. *Mater. Sci. Eng. C* **2013**, *33*, 1963–1968. [[CrossRef](#)]
108. *ISO4287, EN ISO 4287:2000; Geometrical Product Specification (GPS). Surface Texture. Profile Method. Terms, Definitions and Surface Texture Parameters.* British Standards Institution: London, UK, 2000.
109. Smolík, J.; Knotek, P.; Schwarz, J.; Černošková, E.; Janíček, P.; Melánová, K.; Zárbynická, L.; Pouzar, M.; Kutálek, P.; Staněk, J.; et al. 3D micro-structuring by CW direct laser writing on PbO-Bi<sub>2</sub>O<sub>3</sub>-Ga<sub>2</sub>O<sub>3</sub> glass. *Appl. Surf. Sci.* **2022**, *589*, 152993. [[CrossRef](#)]
110. Zhou, S.; Wu, L.; Xiong, M.; He, Q.; Chen, G. Dispersion and UV-VIS Properties of Nanoparticles in Coatings. *J. Dispers. Sci. Technol.* **2005**, *25*, 417–433. [[CrossRef](#)]
111. Ruckerova, A.; Machotova, J.; Svoboda, R.; Pukova, K.; Bohacik, P.; Valka, R. Ambient temperature self-crosslinking latices using low generation PAMAM dendrimers as inter-particle crosslinking agents. *Prog. Org. Coat.* **2018**, *119*, 91–98. [[CrossRef](#)]
112. Machotová, J.; Kalendová, A.; Pitthardová, D.; Steinerová, D.; Stránská, E. Příprava vodou ředitelného samosíťujícího polymerního pojiva s odolností proti bleskové korozi. *Chem. Listy* **2019**, *113*, 745–750.
113. Nirwati, H.; Sinanjung, K.; Fahrnunissa, F.; Wijaya, F.; Napitupulu, S.; Hati, V.P.; Hakim, M.S.; Meliala, A.; Aman, A.T.; Nuryastuti, T. Biofilm formation and antibiotic resistance of *Klebsiella pneumoniae* isolated from clinical samples in a tertiary care hospital, Klaten, Indonesia. *BMC Proc.* **2019**, *13*, 20. [[CrossRef](#)]
114. Bengoechea, J.A.; Sa Pessoa, J. *Klebsiella pneumoniae* infection biology: Living to counteract host defences. *FEMS Microbiol. Rev.* **2018**, *43*, 123–144. [[CrossRef](#)]
115. Huycke, M.M.; Abrams, V.; Moore, D.R. *Enterococcus faecalis* produces extracellular superoxide and hydrogen peroxide that damages colonic epithelial cell DNA. *Carcinogenesis* **2002**, *23*, 529–536. [[CrossRef](#)]

116. Geravand, M.; Fallah, P.; Yaghoobi, M.H.; Soleimanifar, F.; Farid, M.; Zinatizadeh, N.; Yaslianifard, S. Investigation of *Enterococcus faecalis* population in patients with polyp and colorectal cancer in comparison of healthy individuals. *Arq. Gastroenterol.* **2019**, *56*, 141–145. [[CrossRef](#)] [[PubMed](#)]
117. Klasen, H.J. A historical review of the use of silver in the treatment of burns. II. Renewed interest for silver. *Burns* **2000**, *26*, 131–138. [[CrossRef](#)]
118. Yu, Z.; Li, Q.; Wang, J.; Yu, Y.; Wang, Y.; Zhou, Q.; Li, P. Reactive Oxygen Species-Related Nanoparticle Toxicity in the Biomedical Field. *Nanoscale Res. Lett.* **2020**, *15*, 115. [[CrossRef](#)] [[PubMed](#)]
119. Varkey, A.J.; Dlamini, M.D.; Mansuetus, A.B.; Tiruneh, A.T. Germicidal Action of Some Metals/Metal Ions in Combating *E. coli* Bacteria in Relation to Their Electro-Chemical Properties. *J. Water Resour. Prot.* **2013**, *5*, 1132–1143. [[CrossRef](#)]
120. El Sayed, M.T.; El-Sayed, A.S. Biocidal Activity of Metal Nanoparticles Synthesized by *Fusarium solani* against Multidrug-Resistant Bacteria and Mycotoxigenic Fungi. *J. Microbiol. Biotechnol.* **2020**, *30*, 226–236. [[CrossRef](#)]
121. Feng, Q.L.; Wu, J.; Chen, G.Q.; Cui, F.Z.; Kim, T.N.; Kim, J.O. A mechanistic study of the antibacterial effect of silver ions on *Escherichia coli* and *Staphylococcus aureus*. *J. Biomed. Mater.* **2000**, *52*, 662–668. [[CrossRef](#)]
122. Liao, S.Y.; Read, D.C.; Pugh, W.J.; Furr, J.R.; Russell, A.D. Interaction of silver nitrate with readily identifiable groups: Relationship to the antibacterial action of silver ions. *Letts. Appl. Microbiol.* **2003**, *25*, 279–283. [[CrossRef](#)] [[PubMed](#)]
123. Zheng, S.; Bawazir, M.; Dhall, A.; Kim, H.-E.; He, L.; Heo, J.; Hwang, G. Implication of Surface Properties, Bacterial Motility, and Hydrodynamic Conditions on Bacterial Surface Sensing and Their Initial Adhesion. *Front. Bioeng. Biotechnol.* **2021**, *9*, 643722. [[CrossRef](#)] [[PubMed](#)]
124. Yuan, Y.; Hays, M.P.; Hardwidge, P.R.; Kim, J. Surface characteristics influencing bacterial adhesion to polymeric substrates. *RSC Adv.* **2017**, *7*, 14254–14261. [[CrossRef](#)]
125. Samson, R.A.; Houbraken, J.; Thrane, U.; Frisvad, J.C.; Andersen, B. *Food and Indoor Fungi*; CBS-KNAW- Fungal Biodiversity Centre: Utrecht, The Netherlands, 2010; pp. 1–398. ISBN 978-94-91751-18-9.
126. Andersen, B.; Frisvad, J.C.; Søndergaard, I.; Rasmussen, I.S.; Larsen, L.S. Associations between Fungal Species and Water-Damaged Building Materials. *Appl. Environ. Microbiol.* **2011**, *77*, 4180–4188. [[CrossRef](#)]
127. Sharma, D.; Rajput, J.; Kaith, B.S.; Kaur, M.; Sharma, S. Synthesis of ZnO nanoparticles and study of their antibacterial and antifungal properties. *Thin Solid Film.* **2010**, *519*, 1224–1229. [[CrossRef](#)]
128. Eskandari, M.; Haghighi, N.; Ahmadi, V.; Haghighi, F.; Mohammadi, S.H. Growth and investigation of antifungal properties of ZnO nanorod arrays on the glass. *Phys. B Condens. Matter* **2011**, *406*, 112–114. [[CrossRef](#)]
129. Sierra-Fernandez, A.; De La Rosa-García, S.C.; Gomez-Villalba, L.S.; Gómez-Cornelio, S.; Rabanal, M.E.; Fort, R.; Quintana, P. Synthesis, Photocatalytic, and Antifungal Properties of MgO, ZnO and Zn/Mg Oxide Nanoparticles for the Protection of Calcareous Stone Heritage. *ACS Appl. Mater. Interfaces* **2017**, *9*, 24873–24886. [[CrossRef](#)] [[PubMed](#)]